Ore Geology Reviews 137 (2021) 104317

Contents lists available at ScienceDirect

Ore Geology Reviews

journal homepage: www.elsevier.com/locate/oregeorev

Rare earth element enrichment in the ion-adsorption deposits associated granites at Mesozoic extensional tectonic setting in South China

Xu Zhao [a,b], Ning-Bo Li [a,b,*], Jan Marten Huizenga [d,e,f], Shuang Yan [a,b], Yu-Yuan Yang [a,b,c], He-Cai Niu [a,b]

[a] CAS Key Laboratory of Mineralogy and Metallogeny/Guangdong Provincial Key Laboratory of Mineral Physics and Materials, Guangzhou Institute of Geochemistry, Chinese Academy of Sciences, Guangzhou 510640, China
[b] CAS Center for Excellence in Deep Earth Science, Guangzhou 510640, China
[c] University of Chinese Academy of Sciences, Beijing 100049, China
[d] Faculty of Environmental Sciences and Natural Resource Management, Norwegian University of Life Sciences, P.O. Box 5003, NO-1432 Ås, Norway
[e] Economic Geology Research Institute (EGRU), College of Science and Engineering, James Cook University, Townsville, QLD 4811, Australia
[f] Department of Geology, University of Johannesburg, P.O. Box 524, Auckland Park 2006, South Africa

ARTICLE INFO

Keywords:
Rare earth elements
Ion-adsorption
A-type granite
Extensional setting
South China

ABSTRACT

Ion-adsorption type rare earth element mineralization occurs in weathered profile of three Mesozoic granites in the Bachi area, Guangdong Province, South China. In this study, we investigate the REE enrichment processes in these granites using geochemical and geochronological data. The three granites yield zircon U-Pb ages of ca. 189 Ma, 153 Ma and 94 Ma, respectively, and could be divided into Early Jurassic, Late Jurassic and Cretaceous granites. The Early Jurassic and Cretaceous granites show similar geochemical characteristics, i.e. high K_2O and low CaO, Fe_2O_3, and MgO contents, low K_2O/Na_2O ratios, and depletion of Eu, Sr, Ba, Ti, and P. They are characterized by high HFSE (high field strength elements) contents and enriched isotopic compositions with $\varepsilon_{Nd}(t)$ values ranging from −5.4 to-2.7, and $\varepsilon_{Hf}(t)$ values ranging from −4.5 to 1.7. The Late Jurassic granite also shows Eu, Sr, Ba, Ti, and P depletion and high HFSE contents. It has, however, higher CaO, Fe_2O_3, MgO and lower K_2O contents than the Early Jurassic and Cretaceous granites. The Late Jurassic granite also shows more enriched isotopic compositions with $\varepsilon_{Nd}(t)$ values ranging from −9.0 to −8.9, and $\varepsilon_{Hf}(t)$ values ranging from −11.1 to −6.1. In addition, the Late Jurassic granite comprises, in contrast to the Early Jurassic and Cretaceous granites, abundant inherited/captured zircons cores and accessory REE-rich minerals of allanite, titanite, apatite and fluorite. These Mesozoic granites have the geochemical affinity of A-type granite. The Zr saturation temperature is >820 °C for the Early Jurassic and Cretaceous granites, and ~900 °C for the Late Jurassic granite. The Early Jurassic and Cretaceous granites were derived from partial melting of felsic igneous rocks under high-temperature, low-pressure, and anhydrous conditions. The felsic igneous source could provide relatively high REE contents for the melts, and the high-temperature, low-pressure, and anhydrous conditions resulted in residual plagioclase and melting of REE-rich minerals in the source area, which favour to REE enrichment in the melt. The Late Jurassic granite, on the other hand, was derived from a more mafic source and associate with fast crustal magma generation as indicated by its abundant presence of inherited/captured zircon cores in the high-temperature condition. The fast magma generation of the Late Jurassic granite prevented the separation of REE-rich minerals from the melt resulting in REE enrichment. Further, the high-temperature, low-pressure, and anhydrous physicochemical conditions and fast magma generation, which favour to REE enrichment in the granites, are tightly associated with large-scale Mesozoic extension in South China.

* Corresponding author at: Key Laboratory of Mineralogy and Metallogeny, Guangzhou Institute of Geochemistry, Chinese Academy of Sciences, Guangzhou 511 Kehua Street, Tianhe District, Guangzhou 510640, PR China.
E-mail address: liningbo@gig.ac.cn (N.-B. Li).

https://doi.org/10.1016/j.oregeorev.2021.104317
Received 19 February 2021; Received in revised form 23 June 2021; Accepted 23 June 2021
Available online 27 June 2021

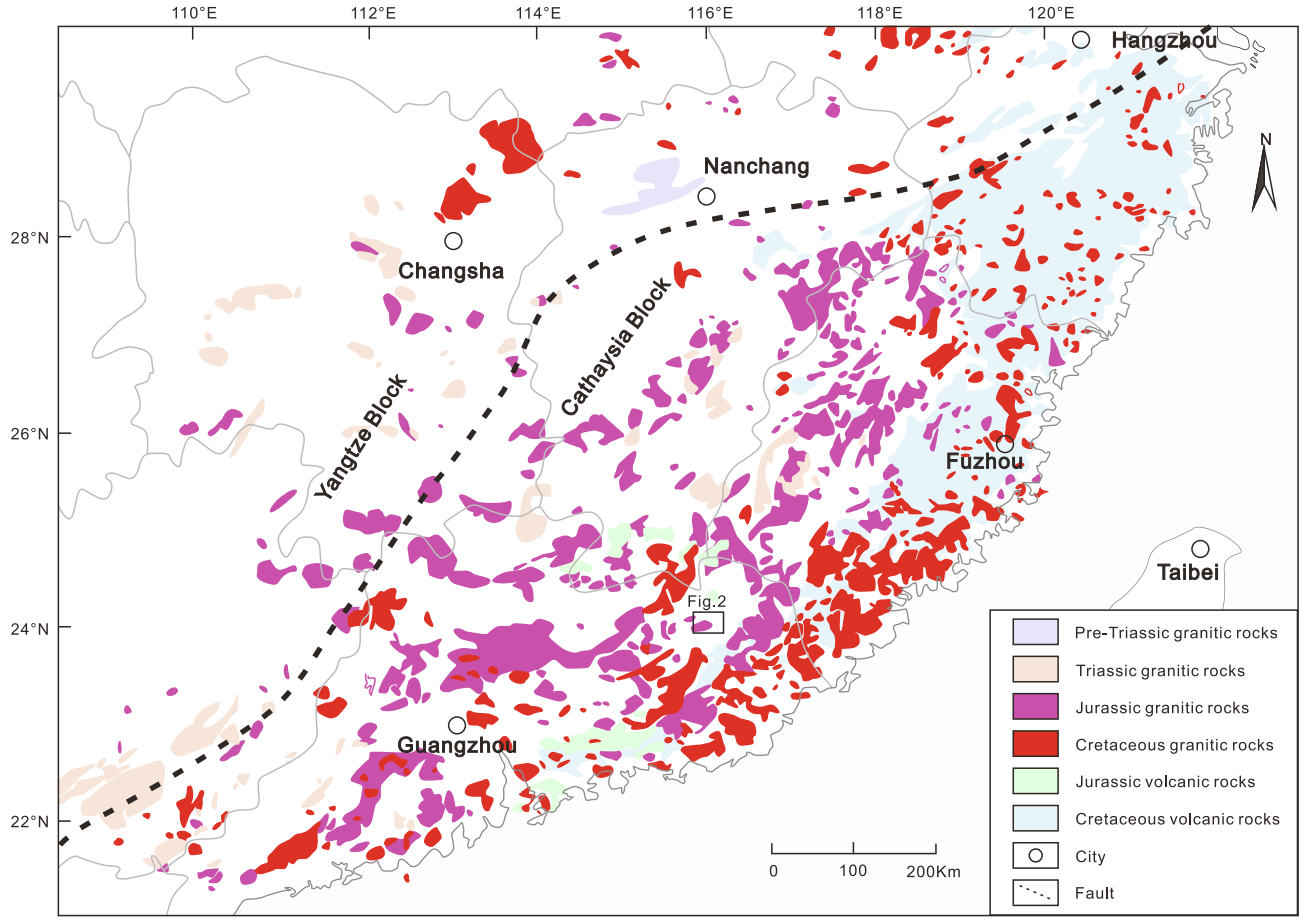

Fig. 1. Geological map of South China showing the spatiotemporal distributions of the Mesozoic igneous and location of the Bachi area, modified after (Chen et al., 2016; Tao et al., 2018).

1. Introduction

Ion-adsorption rare earth elements (REE) deposits are widely distributed in South China (Bao, 1992; Xu et al., 2017; Li et al., 2017; Fu et al., 2019), where they were firstly discovered (i.e. the Zudong deposit in Jiangxi province and the Guposhan deposit in Guangxi province, Xie et al., 2016; Li et al., 2017) in the 1960′s. In recent years, they have also been identified in Southeast Asia (Sanematsu et al., 2013), Madagascar (Janots et al., 2015), the southeastern United States, and Brazil (Rocha et al., 2013). Ion-adsorption REE deposits have gradually become the most important source for the REE, especially for the heavy REE, which are of high economic importance (Xu et al., 2017). They are mostly hosted in the granitic regolith, although a few deposits are also related to rhyolitic tuff lavas (Wang and Ruan, 1989), lamprophyres (Bao and Zhao, 2008), basalts (Zhang et al., 2016), and even metamorphic rocks (Huo, 1992). The supergene weathering processes of these rocks play a crucial role in the alteration of REE minerals, REE mobilization, and REE adsorption on clay minerals (Chi et al., 2005; Bao and Zhao, 2008; Tian et al., 2010). Previous studies focusing on the REE mobility during weathering processes indicate that the REE enrichment, mobilization, and transportation are associated with the dissolution of primary REE-rich minerals such as allanite, titanite, and apatite (Sawka and Chappell, 1988; Li et al., 2017) and involves the formation and re-dissolution of REE-ligand complexes (Wu et al., 1990; Tang and Johannesson, 2010; Yusoff et al., 2013).

Except for supergene weathering processes, the initial REE enrichment of the granites also plays an important role in the formation of ion-adsorption REE deposits. In South China, granites associated with the ion-adsorption deposits usually have high REE contents (Hua et al., 2007; Zhang et al., 2015a, 2015b; Sanematsu and Watanabe, 2016), and the regoliths show REE patterns that are to a largely extent inherited from the parent rocks (Bao and Zhao, 2008; Pei et al., 2015; Li et al., 2017). However, the mechanism of initial REE enrichment in the granites remains controversial. Previous studies on the Guanxi rocks in the Nanling region suggested that the magma source contributed to the REE enrichment in the parent granites (He et al., 2017). Others, however, have proposed that extensive fractional crystallization plays more critical role (Ishihara et al., 2008; Wang et al., 2015). Besides, the South China granites associated with the ion-adsorption REE deposits were mostly formed in the Mesozoic (Zhang et al., 2015b), during which the South China was characterized by long-term extension (Li and Li, 2007). The relationship between regional extension and REE enrichment in South China is still unknown. Therefore, a detailed geochemical study of the parent granites hosting the ion-adsorption REE deposits will shed some light on the influence of the magma source and magma processes on REE enrichment, and their relationship with Mesozoic extension in South China.

Mesozoic granites associated with Ion-adsorption REE mineralization widely occur in the Bachi area in the Guangdong province (Figs. 1 and 2). Here, we present petrological, zircon U-Pb geochronological, elemental, and Sr-Nd-Hf isotopic data of these Mesozoic granites in order to constrain the magma source and magma evolution processes, and the associated REE enrichment. In addition, we establish the relationship between REE enrichment and the Mesozoic extensional tectonic environment in South China.

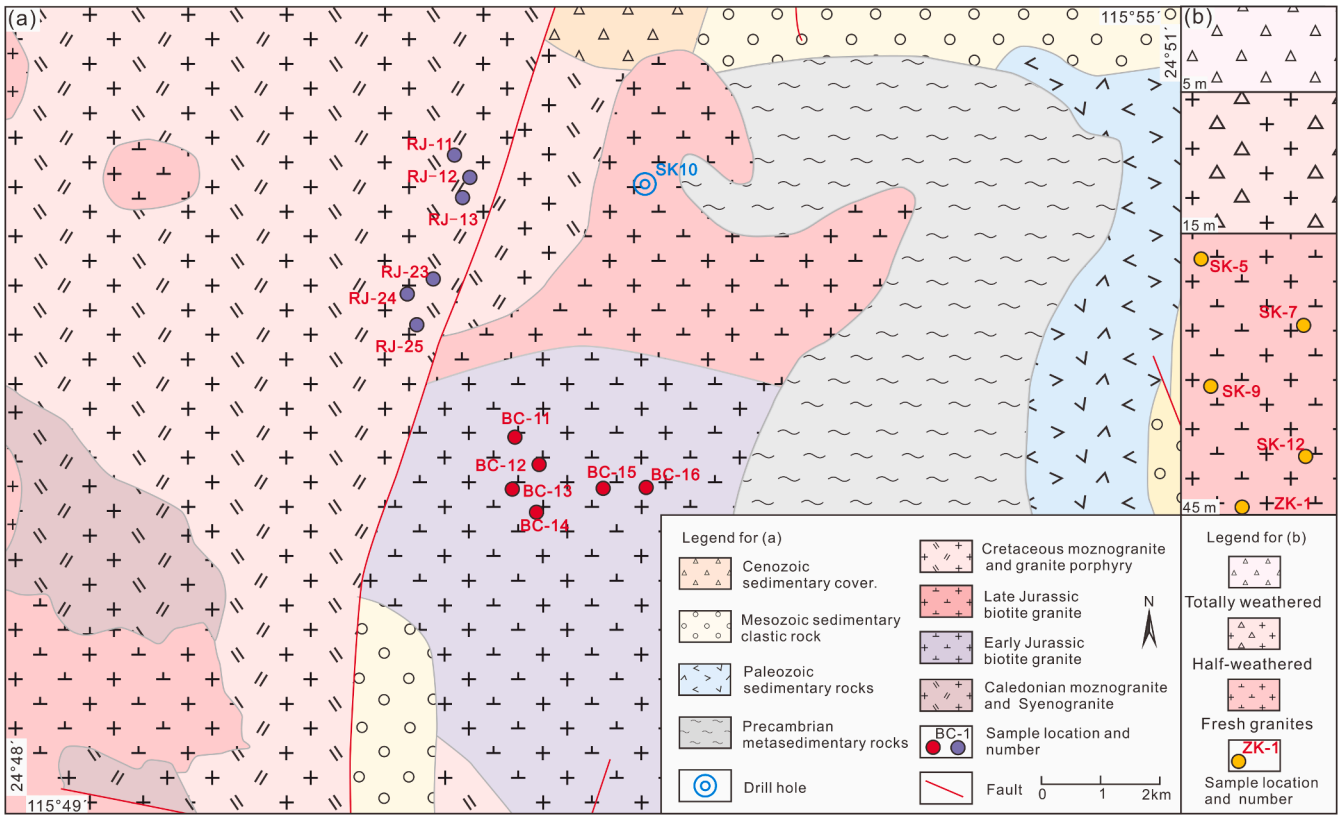

Fig. 2. Simplified geological map of (a) the Bachi area and (b) profile of the drill core of SK10 showing the sample locations.

2. Geological background and petrology

The South China tectonic block is subdivided into the Yangtze block in the northwest and the Cathaysia block in the southeast, which are separated from each other by the Jiangshan-Shaoxin Fault (Fig. 1; Li et al., 2008; Tao et al., 2018). The Cathaysia block contains extensive ion-adsorption type REE deposits (Zhao et al., 2014; Zhang et al., 2015a, 2015b). The Proterozoic sediments exposed in the Cathaysia Block include neritic to bathyal facies flysch formations, silicon-mud formations, and graptolite shale formations, which have been metamorphosed to greenschist-facies and locally up to amphibolite- or granulite facies (Yu et al., 2018). Paleozoic to Mesozoic strata consist of Ordovician flysch-volcanic sequences, folded Late Devonian-Early Triassic shallow marine carbonate-argillaceous-arenaceous sequences, and Late Triassic-Paleocene terrigenous clastic-volcanic rocks. (Chen and Jahn, 1998; Shu, 2006; Tao et al., 2018). The strata are intruded by Mesozoic magmatic rocks, which are dominated by granites varying in age from Jurassic (western interior) to Cretaceous (east coastal areas) (Fig. 1). The granitic rocks generally show high contents of incompatible elements and total alkaline contents and are considered to be A-type granites or highly fractionated granites (Li et al., 2007; Wang et al., 2015). Polymetallic W-Sn-Nb-Ta-REE mineralization is widely present in South China and are associated with the Mesozoic granites, which were formed in an extensional tectonic setting. Mesozoic extension is induced by Jurassic southwestward flat subduction of the Paleo-Pacific Ocean (Li and Li, 2007; Mao et al., 2013; Jiang et al., 2015) and subsequent slab foundering and slab rollback due to an abrupt increase of dip angle of the subducting slab (Zhou et al., 2006; Li et al., 2012; Chen et al., 2016).

The Bachi area is located in the southeast of the Cathaysia Block (Fig. 1). The basement in this region comprises the Sinian metasedimentary rocks including meta-sandstone and slate. Paleozoic to Cenozoic sediments in the Bachi area include conglomerate, sandstone, limestone, and volcanic clastic. Ordovician to Silurian monzogranite and syenogranite intruded in the southwest of the Bachi area. Mesozoic granites, including biotite granite, monzogranite, syenogranite, and granitic porphyry are common (Fig. 2a). In this study, we focus on these Mesozoic granites in the Bachi area that are associated with ion-adsorption REE mineralization.

Drill core samples of gray-red Early Jurassic granite (SK10, Fig. 2b) comprise quartz (35 vol%), K-feldspar/perthite (40 vol%), plagioclase (15 vol%), biotite/chlorite (10 vol%), and accessory zircon, magnetite, and titanite, which is named as biotite granite. The plagioclase phenocrysts (3–4 mm) form subhedral laths and the K-feldspar phenocrysts (up to 10 mm) are usually sub- to euhedral. The biotite has been altered to chlorite (Fig. 3a–c).

The gray-white Late Jurassic granite comprise 1–7 mm sized quartz (40 vol%), plagioclase (15 vol%), K-feldspar (30 vol%), biotite, and chlorite (5 vol%) (Fig. 3d-g), which is also named as biotite granite. The biotite shows different degrees of chlorite alteration. Accessory minerals in the Late Jurassic granite include zircon, allanite, apatite, titanite, fluorite, and magnetite. The allanite usually shows growth zoning, manifesting a magmatic origin. Magnetite and apatite are often associated with allanite (Fig. 3h). Fluorite often occurs as veinlets within the quartz (Fig. 3i).

Outcrop samples of the light-red Cretaceous granite exhibit a porphyritic texture and comprises quartz (20 vol%), K-feldspar (20 vol %), plagioclase (5 vol%), and minor biotite phenocrysts (1–10 mm). indicating it belongs to granite porphyry. The phenocrysts are hosted in a groundmass of quartz (30 vol%) and plagioclase (20 vol%) with accessory magnetite and zircon (<5 vol%) (Fig. 3j–l).

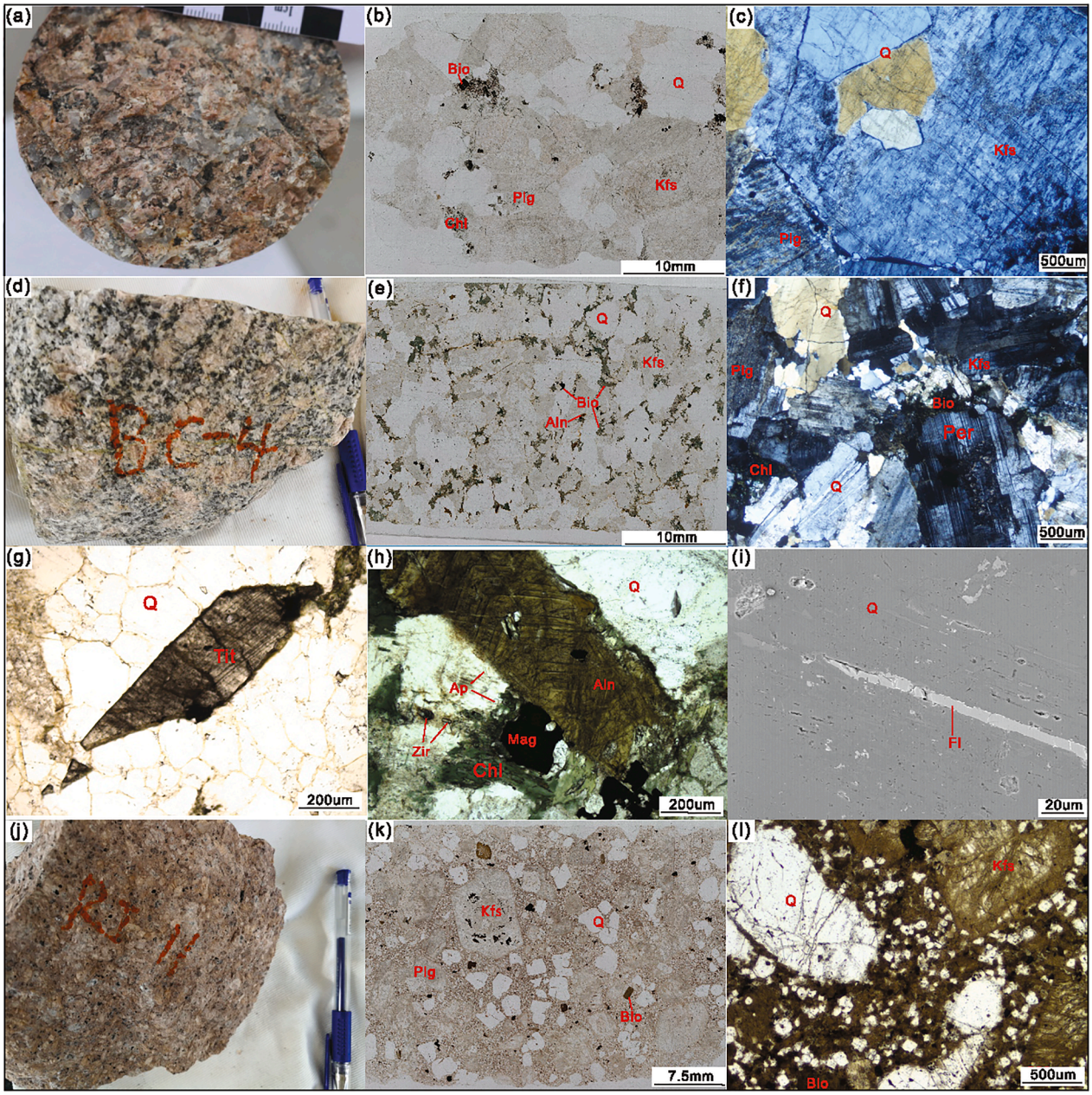

Fig. 3. Hand specimen photos and photomicrographs of (a-c) Early Jurassic, (d-i) Late Jurassic, and (j-l) Cretaceous granites in the Bachi area. Q: quartz; Kfs: K-feldspar; Pl: plagioclase; Per: perthite; Bio: biotite; Chl: chlorite; Aln: allanite; Tit: titanite; Ap: apatite; Zir: zircon; Mag: magnetite; Fl: fluorite.

3. Analytical methods

3.1. Zircon U-Pb dating and in-situ Hf analyses

Zircon grains were separated, handpicked, and mounted in epoxy resin. After polishing and coating, U-Pb dating of zircons was performed at the CAS Key Laboratory of Mineralogy and Metallogeny, Guangzhou Institute of Geochemistry, Chinese Academy of Sciences, Guangzhou, using a 193 nm GeoLasPro and Agilent 7900 ICP-MS with a laser spot size of 29 μm. Cathodoluminescence imaging was done to reveal their internal structures and to identify suitable grains and locations within the grains for U-Pb isotopic analyses. Argon was used as the make-up gas mixed with helium (carrier gas) via a T-connector before entering the ICP. The samples 91,500 zircon and NIST610 glass were used as an external standard for U-Pb dating and trace element calibration, respectively. The calculation of the ages was performed using Isoplot 4.11 (Ludwig, 2003).

In situ Lu-Hf isotope analyses were conducted in dated zircon grains within the same oscillatory zones at the Wuhan Sample Solution Analytical Technology Co. (WSSAT). A Thermo Fisher Neptune Plus MC-ICP-MS equipped with a GeoLas 2005 excimer ArF laser-ablation system was used for the analyses. The sampling-spot size was 44 μm, and the energy density was 15–20 J/cm^2 during the analyses. The standards 91,500 and GJ-1 were analyzed simultaneously. The obtained Hf isotope compositions were 0.282315 ± 0.000014 (1σ) for 91500, and 0.282019 ± 0.000013 (1σ) for GJ-1.

3.2. Whole-rock major and trace element analyses

Major elements analysis of whole rock was conducted using an X-ray fluorescence spectrometry at WSSAT. The error for the major element analysis is <5%. The trace elements were analyzed using an Agilent

Table 1
LA–ICP–MS zircon U–Pb data of the granitic rocks in the Bachi area.

Sample	Th	U	Th/U	U-Th-Pb isotopic ratio								Age (Ma)							
No	ppm			$^{207}Pb/^{206}Pb$	1σ	$^{207}Pb/^{235}U$	1σ	$^{206}Pb/^{238}U$	1σ	$^{208}Pb/^{232}Th$	1σ	$^{207}Pb/^{206}Pb$	1σ	$^{207}Pb/^{235}U$	1σ	$^{206}Pb/^{238}U$	1σ	$^{208}Pb/^{232}Th$	1σ
Early Jurassic biotite granite																			
SK-1	139	117	1.19	0.0517	0.0020	0.2056	0.0074	0.0294	0.0004	0.0096	0.0002	272	89	190	6	187	3	193	5
SK-2	224	434	0.51	0.0520	0.0013	0.2164	0.0055	0.0302	0.0004	0.0103	0.0003	283	56	199	5	192	2	206	5
SK-3	487	885	0.55	0.0508	0.0011	0.2115	0.0047	0.0302	0.0002	0.0101	0.0002	232	45	195	4	192	1	204	4
SK-4	138	222	0.62	0.0514	0.0015	0.2070	0.0062	0.0294	0.0003	0.0099	0.0002	261	69	191	5	187	2	199	5
SK-5	38	79	0.47	0.0481	0.0026	0.2074	0.0101	0.0302	0.0005	0.0104	0.0005	102	131	191	8	192	3	210	10
SK-6	642	882	0.73	0.0542	0.0010	0.2272	0.0060	0.0301	0.0004	0.0095	0.0002	389	38	208	5	191	2	192	3
SK-7	717	1162	0.62	0.0513	0.0008	0.2101	0.0038	0.0296	0.0003	0.0093	0.0002	254	33	194	3	188	2	188	3
SK-8	335	278	1.21	0.0505	0.0017	0.2078	0.0072	0.0298	0.0003	0.0092	0.0002	217	81	192	6	190	2	185	4
SK-9	281	381	0.74	0.0517	0.0013	0.2130	0.0054	0.0300	0.0003	0.0094	0.0002	272	56	196	4	190	2	189	4
SK-10	143	251	0.57	0.0487	0.0025	0.1954	0.0090	0.0294	0.0004	0.0093	0.0004	132	−72	181	8	187	3	188	7
SK-11	389	638	0.61	0.0515	0.0010	0.2109	0.0044	0.0297	0.0003	0.0090	0.0002	265	44	194	4	189	2	180	3
SK-12	301	599	0.50	0.0491	0.0012	0.2009	0.0049	0.0297	0.0002	0.0100	0.0002	154	57	186	4	188	2	202	4
SK-13	279	457	0.61	0.0500	0.0011	0.2045	0.0044	0.0298	0.0003	0.0097	0.0002	195	50	189	4	189	2	194	4
SK-14	286	345	0.83	0.0549	0.0014	0.2270	0.0064	0.0299	0.0003	0.0099	0.0002	409	57	208	5	190	2	199	4
SK-15	1080	1723	0.63	0.0506	0.0007	0.2069	0.0033	0.0296	0.0002	0.0091	0.0001	233	33	191	3	188	2	183	3
SK-16	249	476	0.52	0.0516	0.0012	0.2127	0.0054	0.0299	0.0003	0.0093	0.0002	265	56	196	5	190	2	188	4
SK-17	292	553	0.53	0.0514	0.0010	0.2140	0.0047	0.0301	0.0003	0.0097	0.0002	257	44	197	4	191	2	195	4
SK-18	193	275	0.70	0.0530	0.0017	0.2179	0.0069	0.0300	0.0004	0.0087	0.0003	328	70	200	6	190	2	175	6
SK-19	352	589	0.60	0.0496	0.0012	0.2045	0.0048	0.0300	0.0002	0.0097	0.0002	172	55	189	4	190	1	196	4
SK-20	153	424	0.36	0.0522	0.0014	0.2139	0.0053	0.0299	0.0003	0.0104	0.0003	295	61	197	4	190	2	209	6
Late Jurassic biotite granite (zircon core)																			
BC-3	751	1372	0.55	0.1026	0.0010	2.7559	0.0834	0.1910	0.0051	0.0598	0.0014	398	30	434	6	439	5	422	12
BC-6	82	842	0.10	0.0475	0.0011	0.1596	0.0037	0.0243	0.0002	0.0072	0.0003	189	125	186	7	188	3	183	5
BC-7	131	204	0.64	0.0520	0.0014	0.3195	0.0083	0.0446	0.0004	0.0141	0.0003	1037	64	1013	11	997	10	1007	15
BC-8	493	279	1.77	0.0491	0.0018	0.1657	0.0056	0.0243	0.0004	0.0077	0.0002	254	44	217	7	210	5	154	4
BC-9	167	175	0.95	0.0738	0.0011	1.7117	0.0293	0.1672	0.0017	0.0511	0.0008	1673	18	1344	23	1127	28	1175	26
BC-11	12	1057	0.01	0.0553	0.0007	0.5208	0.0066	0.0680	0.0006	0.0213	0.0010	287	56	282	6	281	3	283	6
BC-19	51	542	0.09	0.0547	0.0008	0.5328	0.0088	0.0705	0.0007	0.0211	0.0006	483	69	428	11	420	5	414	9
BC-25	146	81	1.81	0.0666	0.0016	0.9305	0.0212	0.1021	0.0012	0.0314	0.0008	433	28	426	4	424	4	425	19
BC-30	194	451	0.43	0.0721	0.0008	1.3985	0.0283	0.1395	0.0024	0.0466	0.0007	833	52	668	11	627	7	624	15
BC-36	89	67	1.32	0.0568	0.0017	0.5246	0.0167	0.0673	0.0009	0.0207	0.0005	987	23	888	12	842	14	921	13
BC-39	587	848	0.69	0.0869	0.0008	2.0104	0.0419	0.1669	0.0031	0.0529	0.0008	1367	17	1119	14	995	17	1041	15
Late Jurassic biotite granite (zircon rim)																			
BC-1	189	217	0.87	0.0509	0.0020	0.1719	0.0064	0.0246	0.0003	0.0078	0.0002	239	89	161	6	156	2	156	4
BC-2	293	688	0.43	0.0495	0.0012	0.1658	0.0041	0.0245	0.0004	0.0076	0.0002	58	145	147	3	152	2	155	4
BC-4	229	201	1.14	0.0522	0.0031	0.1712	0.0090	0.0241	0.0005	0.0084	0.0002	124	63	152	4	155	2	163	5
BC-5	243	309	0.79	0.0502	0.0015	0.1656	0.0048	0.0241	0.0003	0.0072	0.0001	172	56	156	4	156	2	154	4
BC-10	1162	1162	1.00	0.0497	0.0011	0.1630	0.0036	0.0237	0.0002	0.0072	0.0001	183	54	153	3	151	1	145	3
BC-13	216	592	0.37	0.0513	0.0010	0.2382	0.0080	0.0331	0.0009	0.0077	0.0002	200	105	148	6	150	2	176	8
BC-14	100	444	0.22	0.0485	0.0013	0.1620	0.0040	0.0243	0.0003	0.0081	0.0002	265	74	160	5	150	2	149	4
BC-15	164	611	0.27	0.0473	0.0014	0.1552	0.0048	0.0237	0.0003	0.0072	0.0003	235	83	156	5	151	2	174	5
BC-16	77	87	0.88	0.0515	0.0037	0.1792	0.0097	0.0239	0.0005	0.0068	0.0003	61	70	147	4	151	2	145	6
BC-18	312	436	0.72	0.0469	0.0012	0.1545	0.0039	0.0241	0.0003	0.0072	0.0002	261	160	167	8	152	3	136	5
BC-21	1913	808	2.37	0.0516	0.0017	0.1707	0.0058	0.0236	0.0002	0.0074	0.0002	95	64	149	4	153	1	165	5
BC-22	90	143	0.63	0.0497	0.0020	0.2009	0.0077	0.0296	0.0004	0.0091	0.0002	195	111	156	6	153	3	150	4
BC-23	169	198	0.85	0.0508	0.0021	0.1699	0.0071	0.0243	0.0004	0.0077	0.0002	287	91	161	6	153	2	140	5
BC-24	190	529	0.36	0.0471	0.0011	0.1555	0.0038	0.0239	0.0003	0.0077	0.0002	206	70	156	4	153	2	145	3
BC-26	158	445	0.35	0.0479	0.0014	0.1577	0.0045	0.0239	0.0002	0.0082	0.0002	295	140	160	8	153	3	169	5
BC-27	167	353	0.47	0.0488	0.0013	0.1621	0.0046	0.0242	0.0003	0.0078	0.0002	43	63	146	3	153	2	146	3
BC-28	279	111	2.52	0.0500	0.0024	0.1665	0.0073	0.0239	0.0005	0.0075	0.0002	139	68	153	4	154	2	158	4

(*continued on next page*)

Table 1 (*continued*)

Sample	Th	U	Th/U	U-Th-Pb isotopic ratio								Age (Ma)							
No	ppm			$^{207}Pb/^{206}Pb$	1σ	$^{207}Pb/^{235}U$	1σ	$^{206}Pb/^{238}U$	1σ	$^{208}Pb/^{232}Th$	1σ	$^{207}Pb/^{206}Pb$	1σ	$^{207}Pb/^{235}U$	1σ	$^{206}Pb/^{238}U$	1σ	$^{208}Pb/^{232}Th$	1σ
BC-31	66	235	0.28	0.0488	0.0023	0.1565	0.0069	0.0236	0.0003	0.0087	0.0004	76	56	150	3	154	1	145	5
BC-32	261	244	1.07	0.0500	0.0017	0.1667	0.0056	0.0243	0.0004	0.0074	0.0002	150	85	156	5	155	2	155	4
BC-33	444	320	1.39	0.0509	0.0018	0.1663	0.0060	0.0237	0.0003	0.0087	0.0003	195	75	157	5	155	2	149	3
BC-35	191	177	1.08	0.0520	0.0020	0.1722	0.0065	0.0240	0.0003	0.0070	0.0002	232	62	159	6	155	3	154	4
Late Cretaceous granite porphyry																			
RJ-1	481	461	1.04	0.0487	0.0013	0.0971	0.0028	0.0145	0.0002	0.0046	0.0001	200	60	94	3	93	1	92	2
RJ-2	418	352	1.19	0.0456	0.0014	0.0917	0.0030	0.0146	0.0002	0.0047	0.0001	/	/	89	3	93	1	95	2
RJ-3	179	110	1.63	0.0464	0.0028	0.1033	0.0051	0.0144	0.0002	0.0047	0.0001	17	150	100	5	92	1	95	3
RJ-4	273	266	1.03	0.0495	0.0017	0.0995	0.0034	0.0147	0.0002	0.0047	0.0001	169	84	96	3	94	1	95	2
RJ-5	222	194	1.14	0.0466	0.0025	0.0983	0.0052	0.0149	0.0003	0.0045	0.0001	28	126	95	5	95	2	91	3
RJ-6	169	100	1.70	0.0472	0.0028	0.1050	0.0053	0.0145	0.0003	0.0046	0.0001	58	133	101	5	93	2	93	3
RJ-7	215	193	1.12	0.0509	0.0021	0.0997	0.0039	0.0145	0.0002	0.0044	0.0001	235	66	96	4	93	1	89	2
RJ-8	420	407	1.03	0.0480	0.0014	0.0959	0.0028	0.0146	0.0002	0.0045	0.0001	98	67	93	3	93	1	90	2
RJ-9	332	350	0.95	0.0485	0.0016	0.0966	0.0034	0.0145	0.0002	0.0045	0.0001	124	86	94	3	93	1	92	2
RJ-10	589	492	1.20	0.0471	0.0014	0.0941	0.0028	0.0146	0.0002	0.0046	0.0001	54	67	91	3	93	1	93	2
RJ-11	374	367	1.02	0.0498	0.0018	0.1010	0.0037	0.0148	0.0002	0.0048	0.0001	187	81	98	3	95	1	97	2
RJ-12	775	658	1.18	0.0473	0.0011	0.0944	0.0024	0.0145	0.0002	0.0047	0.0001	65	54	92	2	93	1	96	2
RJ-13	167	137	1.22	0.0504	0.0026	0.1049	0.0046	0.0146	0.0002	0.0044	0.0001	213	114	101	4	93	1	89	3
RJ-14	173	197	0.88	0.0495	0.0020	0.1007	0.0042	0.0148	0.0002	0.0046	0.0001	169	94	97	4	95	1	93	3
RJ-15	187	187	1.00	0.0528	0.0021	0.1063	0.0041	0.0146	0.0002	0.0049	0.0001	320	90	103	4	94	1	99	3
RJ-16	338	145	2.33	0.0502	0.0026	0.1029	0.0050	0.0146	0.0002	0.0047	0.0001	211	122	99	5	93	2	95	2
RJ-17	436	223	1.95	0.0506	0.0023	0.1006	0.0045	0.0145	0.0002	0.0049	0.0001	220	101	97	4	93	1	98	2
RJ-18	131	110	1.19	0.0484	0.0027	0.1024	0.0050	0.0146	0.0003	0.0046	0.0001	117	126	99	5	94	2	93	3
RJ-19	361	377	0.96	0.0480	0.0013	0.0958	0.0026	0.0146	0.0002	0.0047	0.0001	98	67	93	2	93	1	95	2
RJ-20	279	260	1.07	0.0547	0.0022	0.1101	0.0042	0.0145	0.0002	0.0050	0.0001	398	91	106	4	93	1	100	2
RJ-21	541	198	2.73	0.0450	0.0035	0.0903	0.0075	0.0145	0.0002	0.0048	0.0001	/	/	88	7	93	2	96	3
RJ-22	165	157	1.05	0.0462	0.0021	0.0924	0.0040	0.0148	0.0003	0.0047	0.0001	6	117	90	4	95	2	96	3
RJ-23	534	476	1.12	0.0453	0.0030	0.0899	0.0057	0.0145	0.0003	0.0047	0.0002	/	/	87	5	93	2	95	3

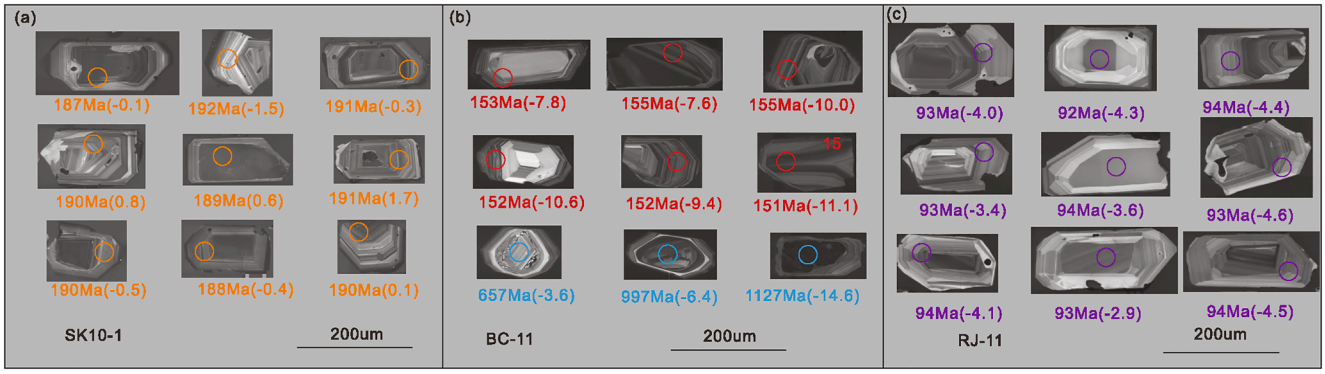

Fig. 4. Representative cathodoluminescence images of zircon grains with the locations of U-Pb (solid circle) and Hf (dotted circle) isotopic analysis for (a) Early Jurassic, (b) Late Jurassic, and (c) Cretaceous granites in the Bachi area. The numbers before the brackets are the U-Pb ages and within the brackets are the $\varepsilon_{Hf}(t)$ values.

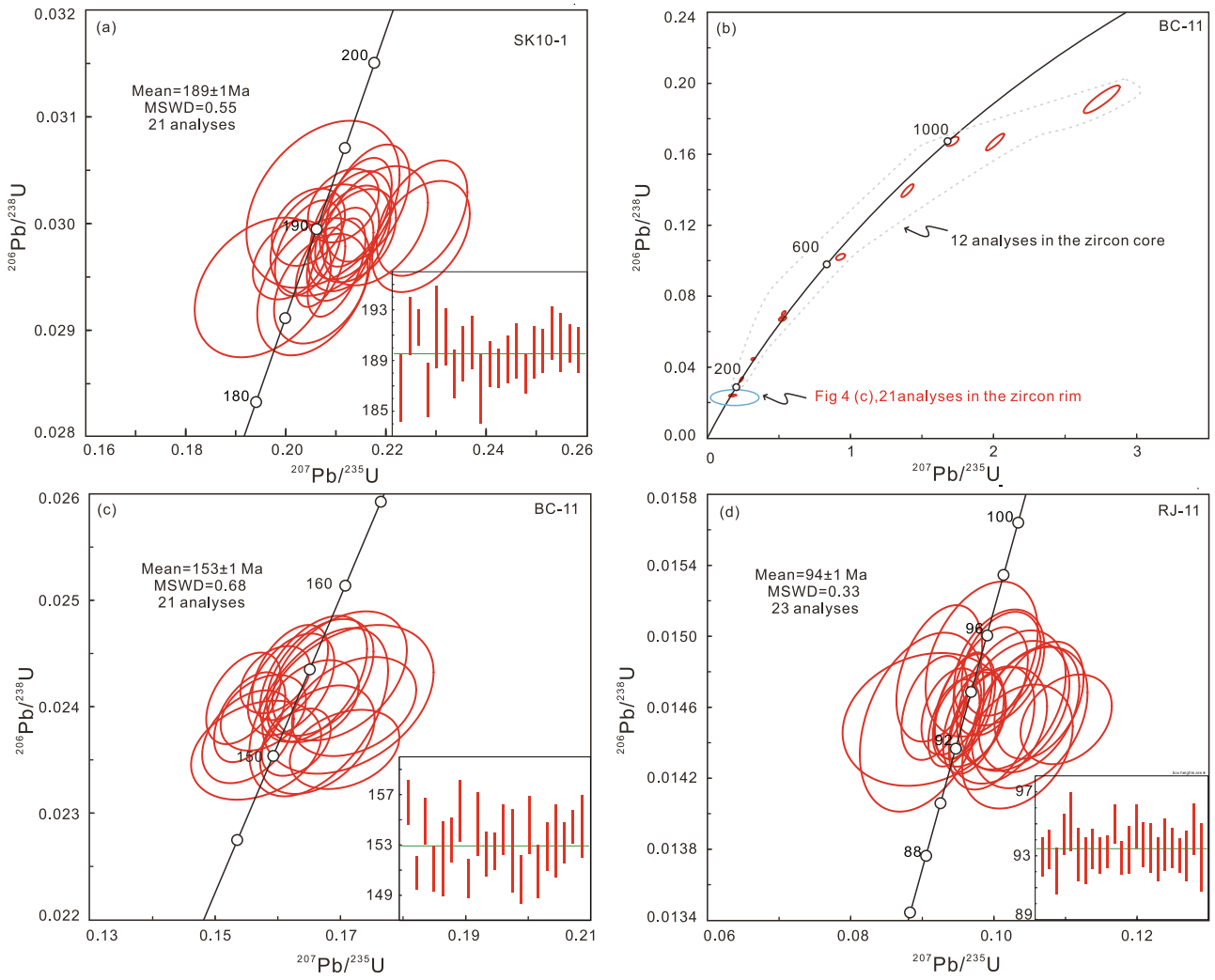

Fig. 5. Zircon concordia plots and bar charts for the (a) Early Jurassic, (b-c) Late Jurassic, and (d) Cretaceous granites.

7700e ICP-MS at WSSAT. The sample powder was weighed and placed in a Teflon bomb after drying of 12 h in an oven at 105 °C. The sample powders were digested in a HF + HNO_3 solution in Teflon bombs, which were subsequently put in a stainless-steel pressure jacket and heated to 190 °C in an oven for >24 h. The final solution was transferred to a polyethylene bottle and diluted to 100 g using 2% HNO_3 as a dilutant. The error for the trace element analysis is <2%.

3.3. Whole-rocks Sr-Nd isotope analyses

Sr-Nd isotopic compositions were analyzed using a Thermo Fisher Neptune Plus MC-ICP-MS at WSSAT. Isotope separation was conducted using cation exchange techniques. The detection limit of Sm and Nd is 0.05 ng, and 0.20 ng for Rb and Sr. Analyses of the NIST SRM 987 standard solution yielded $^{87}Sr/^{86}Sr$ ratios of 0.710244 ± 22 (2σ, n = 32),

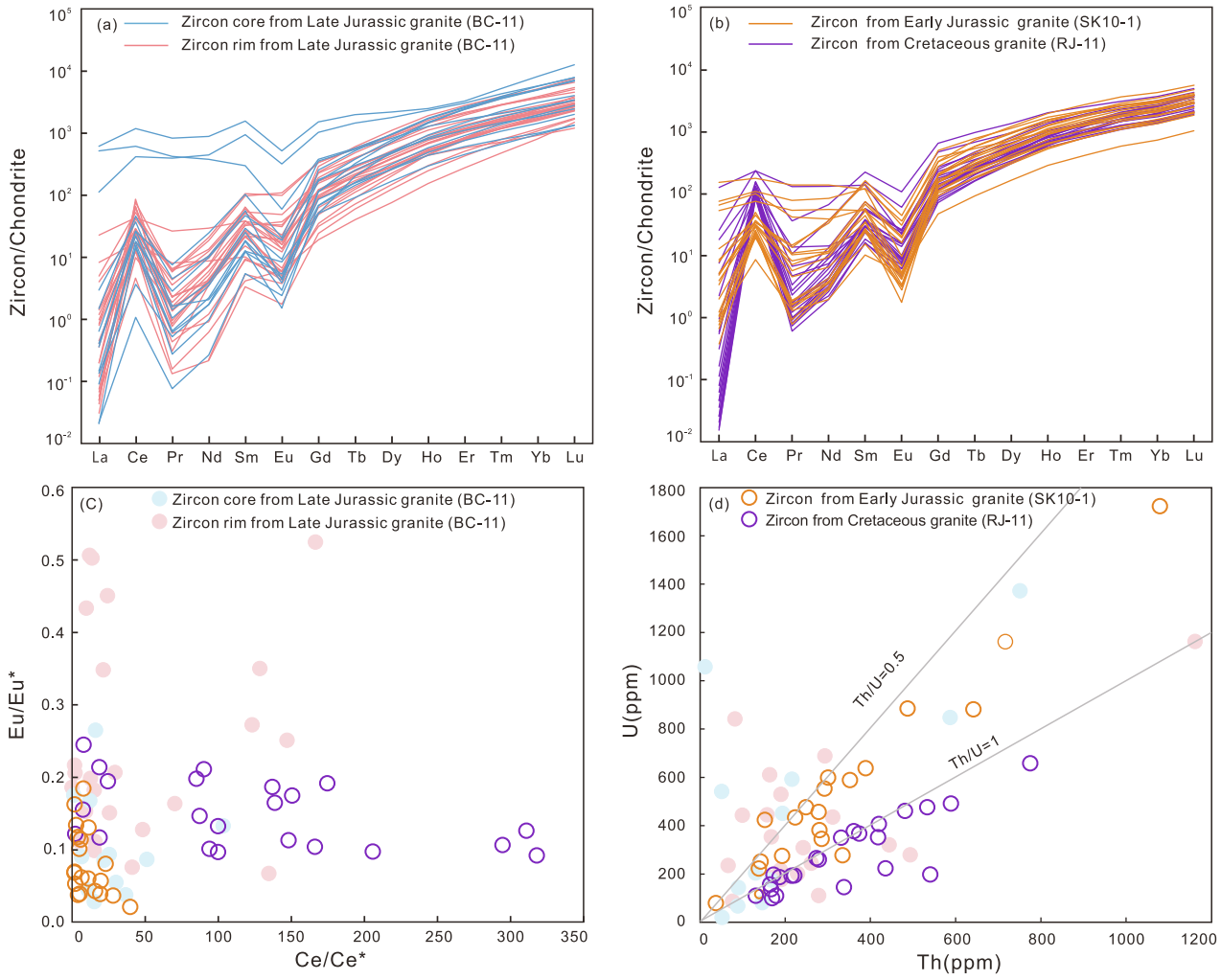

Fig. 6. (a-b) Zircon REE patterns, (c) Zircon Eu/Eu* vs. Ce/Ce* and, (d) Zircon U vs. Th for the Mesozoic granites in the Bachi area.

which is within error of their published values (0.710241 ± 12, Thirlwall, 1991). In addition, the USGS reference materials BCR-2 (basalt) and RGM-2 (rhyolite) yielded results of 0.705034 ± 14 (2σ, n = 4) and 0.704192 ± 10 (2σ, n = 4) for $^{87}Sr/^{86}Sr$, respectively. Analyses of the JNdi-1 standard yielded $^{143}Nd/^{144}Nd$ ratio of 0.512118 ± 15 (2σ, n = 31), which is within error to their published values (0.512115 ± 07, Tanaka et al., 2000). The JNdi-1 standard was measured after every ten samples. In addition, the USGS reference materials BCR-2 (basalt) and RGM-2 (rhyolite) yielded $^{143}Nd/^{144}Nd$ results of 0.512644 ± 15 (2σ, n = 6) and 0.512810 ± 15 (2σ, n = 4), respectively. The errors for the $^{87}Rb/^{86}Sr$ and $^{147}Sm/^{144}Nd$ values are <1% and <0.5%, respectively.

4. Results

4.1. Zircon U-Pb dating

Cathodoluminescence images and U-Pb isotopic data for the zircon grains in the Mesozoic granites from the Bachi area are presented in Table 1 and Figs. 4–6. The colorless zircon grains from the Early Jurassic granite show mostly ellipsoidal shapes with lengths between 100 and 250 μm (length–width ratios between 1 and 4) (Fig. 4a). The grains exhibit clear oscillatory zoning with high Th/U mass ratios of 0.47–1.20 (Fig. 6d), indicative of magmatic zircons (Hoskin and Schaltegger, 2003; Yang et al., 2014). All data plot close to concordia line yielding $^{238}U/^{206}Pb$ ages between 187 and 192 Ma with a weighted mean age of 189 ± 1 Ma (MSWD = 0.55, Fig. 5a). The zircon REE patterns for the Early Jurassic granite are scattered and show negative Eu and positive Ce anomalies (Fig. 6b).

Euhedral columnar shaped zircon grains from Late Jurassic granite are light yellow to colorless with lengths between 100 and 200 μm and length–width ratios between 1 and 3. Most zircons show clear oscillatory zoning and some zircons also show clear core-and-rim texture (Fig. 4b). The zircon cores show variable Th/U mass ratios (0.01–1.31) with $^{238}U/^{206}Pb$ ages ranging between 210 and 1127 Ma (Fig. 5b). The cores show features of metamorphic zircons without oscillatory zoning, which may have been inherited from the magmatic source or captured during magma ascend. The zircon cores display more consistent Eu/Eu* and Ce/Ce* ratios than the zircon rims (Fig. 6a). The zircon rims with clear oscillatory zoning display Th/U mass ratios between 0.22 and 2.51 (mostly higher than 0.5, Fig. 6d) and yield $^{238}U/^{206}Pb$ ages ranging between 150 and 156 Ma. The data plot near the concordia line with weighted mean age of 153 ± 0.9 Ma (MSWD = 0.68), which is interpreted as the emplacement age of the Late Jurassic granite.

Colorless prismatic euhedral zircon grains in the Cretaceous granite have variable lengths (150–400 μm) and aspect ratios (1–4) (Fig. 4c). The grains exhibit clear oscillatory zoning and have high Th/U mass ratios (0.87–2.73, Fig. 6d). The $^{238}U/^{206}Pb$ ages range between 92 and 95 Ma, with a weighted mean intrusion age of 94 ± 1 Ma (MSWD = 0.33) (Fig. 5d). The zircons from Cretaceous granite show similar REE patterns as the zircons from Early Jurassic granite and the zircon rims from Late Jurassic granite (Fig. 6a, b), but do show more variable Ce/Ce* ratios (Fig. 6c).

Table 2
Whole rocks major (wt%) and trace elements (ppm) for the samples from the granitic rocks in the Bachi area.

Samples	SK-5	SK-7	SK-9	SK-12	ZK-1	BC-11	BC-12	BC-13	BC-14	BC-15	BC-16	RJ-11	RJ-12	RJ-13	RJ-23	RJ-24	RJ-25
	Early Jurassic Biotite granite					Late Jurassic Biotite granite						Late Cretaceous granite porphyry					
SiO_2	76.0	75.0	74.8	76.7	75.8	72.9	71.2	71.5	70.8	70.1	72.6	73.1	73.1	71.4	76.5	75.1	74.5
TiO_2	0.20	0.17	0.17	0.16	0.13	0.51	0.60	0.54	0.58	0.54	0.53	0.31	0.29	0.32	0.20	0.25	0.26
Al_2O_3	12.5	13.3	13.2	12.4	12.6	12.8	13.4	13.4	13.3	14.1	13.0	14.1	14.4	15.3	12.6	12.7	12.9
$Fe_2O_3^T$	1.37	1.34	1.19	1.43	1.47	3.42	3.99	3.27	3.74	3.60	3.68	1.48	1.53	1.45	1.24	1.36	1.36
MnO	0.01	0.01	0.01	0.02	0.02	0.07	0.08	0.07	0.08	0.08	0.08	0.04	0.03	0.05	0.02	0.02	0.02
MgO	0.14	0.28	0.15	0.28	0.24	0.78	0.86	0.83	0.81	0.73	0.83	0.30	0.24	0.26	0.21	0.14	0.15
CaO	0.17	0.14	0.18	0.20	0.39	1.48	2.63	1.45	2.03	2.31	1.89	0.07	0.07	0.05	0.04	0.10	0.10
Na_2O	3.52	3.08	3.32	3.32	3.45	2.82	2.92	3.08	3.42	2.69	2.85	1.58	1.63	0.69	0.36	0.52	0.51
K_2O	5.24	6.08	5.70	5.23	5.39	4.07	3.26	4.58	3.91	4.86	3.70	7.55	7.42	7.77	7.54	8.93	9.71
P_2O_5	0.03	0.02	0.02	0.02	0.02	0.16	0.19	0.16	0.18	0.17	0.17	0.03	0.02	0.02	0.02	0.02	0.02
LOI	0.59	0.86	0.62	0.59	0.62	1.04	0.96	0.87	0.93	0.80	0.88	1.37	1.61	2.45	1.49	0.71	0.77
SUM	99.7	100.3	99.4	100.3	100.1	100.1	100.0	99.8	99.8	100.0	100.2	99.9	100.3	99.8	100.2	99.9	100.3
A/CNK	1.06	1.12	1.10	1.08	1.03	1.09	1.02	1.06	0.98	1.02	1.07	1.29	1.32	1.58	1.42	1.19	1.12
A/NK	1.09	1.14	1.14	1.11	1.09	1.42	1.60	1.34	1.35	1.46	1.50	1.30	1.34	1.60	1.43	1.21	1.14
Li	4.1	5.3	3.3	6.2	11.0	11.4	17.5	11.8	14.4	16.0	12.5	35.1	31.1	33.0	31.9	220.4	177.0
Be	3.79	2.74	2.23	2.36	2.84	3.44	3.55	3.41	3.19	3.49	3.65	2.14	2.12	1.88	2.61	3.26	3.72
Sc	2.68	2.16	2.16	1.64	1.56	7.35	8.76	7.14	8.34	7.71	7.31	3.29	3.42	3.76	2.30	2.16	1.83
V	7.48	6.61	6.75	5.88	6.01	38.29	49.31	37.77	49.07	47.10	43.27	5.86	4.97	5.39	5.82	4.73	4.98
Cr	0.95	0.90	1.52	0.72	1.32	1.94	2.65	2.53	2.34	2.28	2.75	0.74	0.63	0.41	1.64	0.98	0.86
Co	0.75	1.04	0.44	0.88	0.79	4.80	4.83	5.07	4.92	4.84	4.69	0.29	0.25	0.29	0.28	0.31	0.23
Ni	0.84	1.12	0.61	1.01	0.77	1.39	1.62	2.38	1.72	1.64	1.57	0.83	1.39	1.86	1.21	0.88	0.62
Cu	3.08	1.15	1.07	0.84	0.70	2.37	3.14	7.46	1.27	2.87	15.76	0.59	0.44	0.40	0.70	0.81	0.53
Zn	11.3	24.0	13.7	28.3	36.5	57.1	69.1	53.3	59.1	65.2	56.9	62.0	55.3	56.1	37.9	53.1	43.0
Ga	19.5	22.9	20.6	20.1	21.5	18.3	20.2	17.5	19.4	19.7	18.8	22.1	21.8	23.0	20.4	20.1	20.2
Rb	180	226	195	176	229	130	109	138	116	164	113	284	279	288	371	389	407
Sr	52	48	55	46	32	262	282	307	313	249	262	21	22	18	23	24	23
Y	48.9	37.0	43.2	34.7	52.8	45.6	51.4	57.2	56.0	48.6	50.3	175.6	144.5	137.3	101.1	55.8	54.6
Zr	217	156	169	153	158	264	318	275	295	277	293	352	318	337	177	218	244
Nb	41.6	26.0	37.2	28.4	45.8	27.6	30.7	27.2	32.3	27.5	27.3	33.5	32.5	34.7	44.7	37.0	38.1
Sn	2.79	3.79	3.56	3.60	4.11	3.90	4.24	3.69	3.72	3.34	3.79	3.08	2.88	3.26	4.48	3.58	3.70
Cs	2.36	3.65	2.28	2.29	4.72	0.86	0.88	0.80	0.37	1.56	0.86	4.01	3.80	4.01	3.31	2.72	2.81
Ba	435.8	461.4	497.8	393.8	302.7	828.0	712.1	1053.8	853.6	1033.8	769.0	97.3	84.5	89.7	89.3	53.4	57.5
La	88.0	65.5	74.2	56.1	57.3	73.2	79.7	76.0	91.4	85.1	77.2	273.2	203.2	184.6	85.8	68.0	77.8
Ce	170	127	143	104	112	139	150	146	174	143	150	293	289	281	110	135	135
Pr	19.2	14.2	16.4	12.0	13.1	16.1	17.4	16.6	19.7	18.3	16.9	62.8	46.5	41.1	19.9	18.1	19.4
Nd	66.2	48.6	57.6	41.7	47.0	57.8	61.8	58.9	71.7	63.6	60.1	222.0	167.0	148.2	69.2	65.8	72.0
Sm	13.8	9.7	11.9	8.5	10.7	11.0	12.2	11.3	13.8	12.8	11.6	52.6	37.5	33.2	17.6	15.9	17.4
Eu	1.12	0.95	1.17	0.92	0.74	1.44	1.57	1.60	1.72	1.77	1.46	4.60	3.30	3.00	1.16	0.99	1.02
Gd	10.67	7.48	10.37	7.48	10.29	9.36	10.25	9.82	11.02	10.40	9.48	49.85	35.04	32.53	18.22	12.89	14.30
Tb	1.56	1.18	1.46	1.11	1.58	1.35	1.56	1.47	1.72	1.54	1.38	7.04	5.27	4.92	3.11	1.99	2.09
Dy	9.12	6.95	8.56	6.61	9.58	7.95	8.91	8.89	9.88	8.98	8.07	36.87	28.43	26.59	17.75	11.16	11.29
Ho	1.77	1.30	1.55	1.23	1.82	1.59	1.79	1.84	2.04	1.72	1.71	6.41	5.05	4.87	3.44	2.09	2.03
Er	4.71	3.55	3.99	3.35	5.06	4.38	4.90	5.21	5.41	4.56	4.53	14.69	11.83	11.26	9.06	5.36	5.01
Tm	0.67	0.52	0.58	0.46	0.75	0.63	0.71	0.73	0.74	0.64	0.64	1.88	1.49	1.42	1.27	0.70	0.66
Yb	4.17	3.40	3.74	2.92	4.84	4.02	4.50	4.47	4.89	3.89	4.15	11.10	8.69	8.44	7.75	4.24	4.07
Lu	0.60	0.49	0.56	0.42	0.69	0.57	0.66	0.64	0.68	0.55	0.61	1.50	1.24	1.17	1.10	0.59	0.56
Hf	7.20	5.33	5.89	5.41	6.28	7.23	8.56	7.35	7.85	7.25	7.90	9.58	8.94	9.63	6.12	6.71	7.28
Ta	2.87	3.08	3.16	1.98	3.40	2.50	2.55	2.38	2.90	2.21	2.32	2.33	2.21	2.33	3.16	2.69	2.77
Tl	0.88	1.20	1.07	0.85	1.14	0.62	0.53	0.63	0.56	0.86	0.54	1.44	1.30	1.43	2.43	2.12	2.15
Pb	14.2	18.5	17.6	24.8	20.0	24.8	23.7	26.3	20.0	29.9	25.6	33.6	31.9	33.0	25.2	31.2	32.6
Th	32.3	35.5	27.8	23.4	31.9	32.3	34.5	32.9	37.5	29.6	33.2	36.4	36.2	40.8	42.5	34.8	33.5
U	2.59	3.83	2.06	3.79	7.74	4.81	7.48	5.50	3.81	4.75	3.22	4.47	3.42	3.66	7.98	2.84	2.83
REE + Y	441	327	379	281	328	375	408	400	465	405	398	1213	988	920	466	398	417
Ce/Ce*	1.01	1.02	1.01	0.98	1.00	1.00	0.99	1.01	1.01	0.89	1.02	0.55	0.73	0.79	0.65	0.94	0.85
Eu/Eu*	0.27	0.33	0.31	0.34	0.21	0.42	0.42	0.45	0.41	0.46	0.41	0.27	0.27	0.28	0.20	0.20	0.19
$(La/Yb)_N$	15.15	13.81	14.25	13.77	8.49	13.08	12.70	12.21	13.41	15.72	13.34	17.65	16.78	15.68	7.94	11.50	13.71
T_{Zr}(°C)	866	836	843	834	833	886	899	887	887	883	895	927	918	933	862	873	881

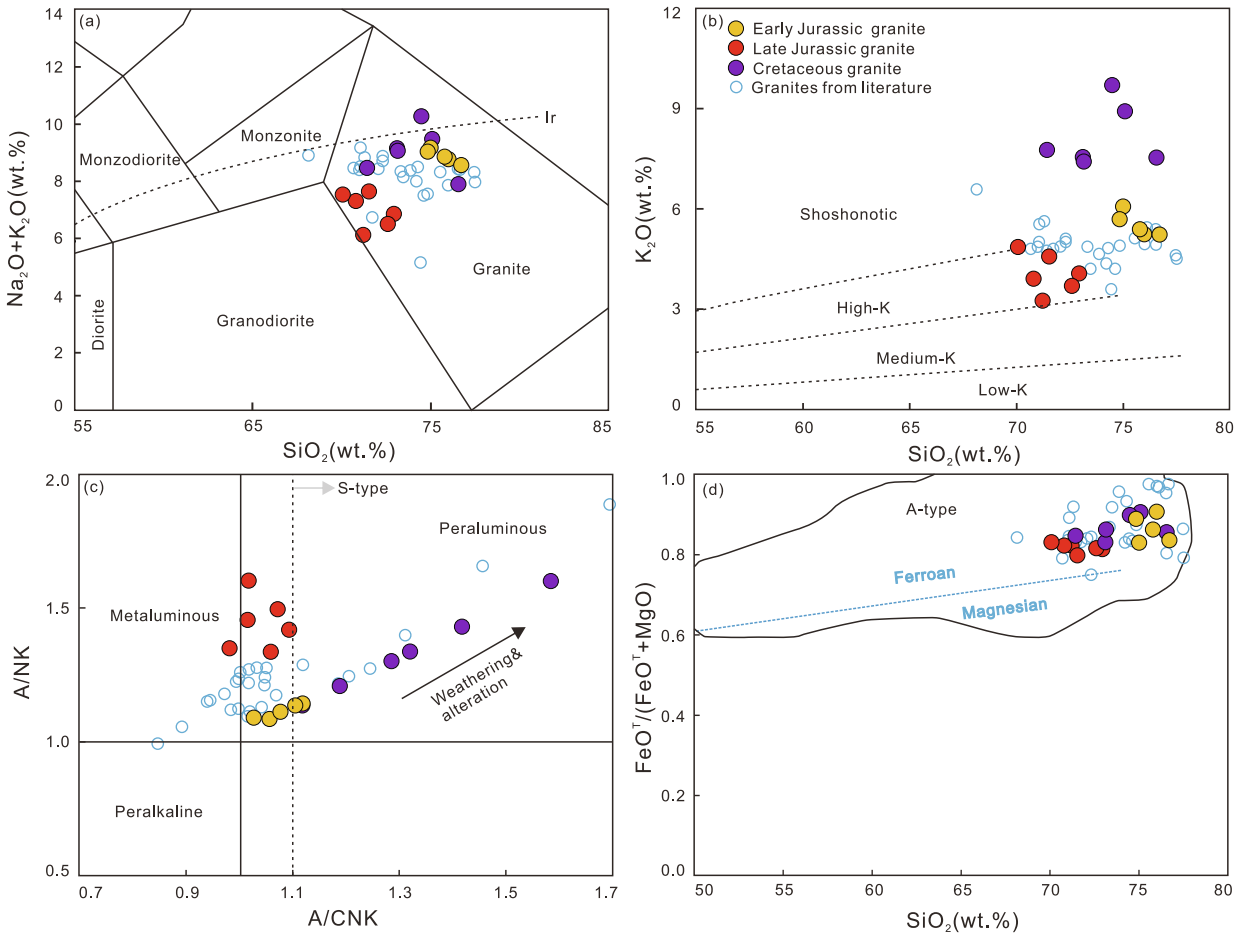

Fig. 7. Diagrams of (a) total alkaline ($Na_2O + K_2O$) vs. SiO_2 (Wilson, 1989), (b) K_2O vs. SiO_2 (Middlemost, 1985), (c) A/NK vs. A/CNK (Maniar and Piccoli, 1989) and (d) $FeO^T/(FeO^T + MgO)$ vs. SiO_2 (Frost et al., 2001) for the Mesozoic granites in the Bachi area. A/NK is the molar ratio of $Al_2O_3/(Na_2O + K_2O)$, A/CNK is the molar ratio of $Al_2O_3/(CaO + Na_2O + K_2O)$. The data for the granites form the literature are from Li et al. (2003), Wang et al (2015) and He et al (2017).

4.2. Whole-rock geochemical characteristics

The data for whole rock major and trace elements are listed in Table 2 and illustrated in Figs. 7–9. All samples from the three Mesozoic granites show SiO_2 contents >70.0 wt% and are classified as subalkaline granites (Fig. 7a). The Late Jurassic granite samples plot in the field of high-K calc-alkaline granite (Fig. 7b) and show lower K_2O contents and K_2O/Na_2O ratios than those of the Early Jurassic and Cretaceous granites, which are classified as high-K calc-alkaline to shoshonotic granite (Fig. 7b), but all of them are aluminous with A/NK > 1 (Fig. 7c). Besides, the Late Jurassic granite displays higher TiO_2, Fe_2O_3, MgO, P_2O_5 and CaO contents than those of the Early Jurassic and Cretaceous granites (Fig. 8), but they all have similar and high $FeO^T/(FeO^T + MgO)$ ratios, and are classified as a ferroan A-type granite (Fig. 7d).

Generally, these granites all show (1) Eu depletion (Eu/Eu* ratios between 0.19 and 0.46), (2) slight enrichment of the light REEs with $(La/Yb)_N$ ratios between 7.94 and 17.65 (Fig. 9a), and (3) Ba, Nb, Ta, Sr, P, and Ti depletion (Fig. 9b). However, the Cretaceous granite shows a negative Ce anomaly in contrast to the Early Jurassic and Late Jurassic granites (Fig. 9a).

Some of the Cretaceous granite samples have high loss on ignition values (up to 2.45 wt%), suggesting that they underwent alteration after emplacement. These samples with high LOI values are characterized by negative Ce anomalies (Ce/Ce* < 0.9), confirming alteration (Polat and Hofmann, 2003; Zhao et al., 2019), which is also evidenced by their variable A/CNK ratios (Fig. 7c). The mobile elements (K, Sr, and Ba) contents may have changed during the alteration. Therefore, these elements and the Sr isotopic composition from the Cretaceous granite were excluded in the discussion on the magmatic processes. Some Cretaceous granite samples show low LOI values (0.71–0.77 wt%) and no obvious Ce anomaly (Ce/Ce* = 0.94), indicating no or minor alteration. The Early Jurassic and Late Jurassic granites show low LOI values (0.59–1.04 wt%), no obvious Ce anomaly (Ce/Ce* = 0.92–1.02), and consistent elemental compositions (Fig. 9), indicating insignificant alteration.

4.3. Whole-rock Sr-Nd isotope results

The data for whole rocks Sr-Nd isotopic compositions are present in Table 3 and illustrated in Fig. 10a, b. The Early Jurassic granite displays $(^{86}Sr/^{87}Sr)_i$ ratios of 0.705861–0.706813, $\varepsilon_{Nd}(t)$ values of −3.0 to −2.7 with Nd-T_{DM2} values between 1247 and 1307 Ma. The Late Jurassic granite shows more enriched Sr-Nd isotopic compositions with $(^{86}Sr/^{87}Sr)_i$ ratios of 0.712784–0.713244, $\varepsilon_{Nd}(t)$ values of −9.0 to −8.9 with Nd-T_{DM2} range of 1661–1674 Ma. The Cretaceous granite also shows consistent Nd isotopic values with $\varepsilon_{Nd}(t)$ values between −5.4 and −5.2 and Nd-T_{DM2} ranging between 1316 and 1335 Ma.

4.4. Zircon Hf isotope results

Zircon Hf isotopic data are shown in Table 4. The zircons from Early Jurassic granite show consistent Hf isotopic compositions with $^{176}Hf/^{177}Hf$ ratios of 0.282557–0.282709 and $\varepsilon_{Hf}(t)$ values of −3.9–1.7. The Hf-T_{DM2} values range between 1004 and 1316 Ma. Zircon cores from

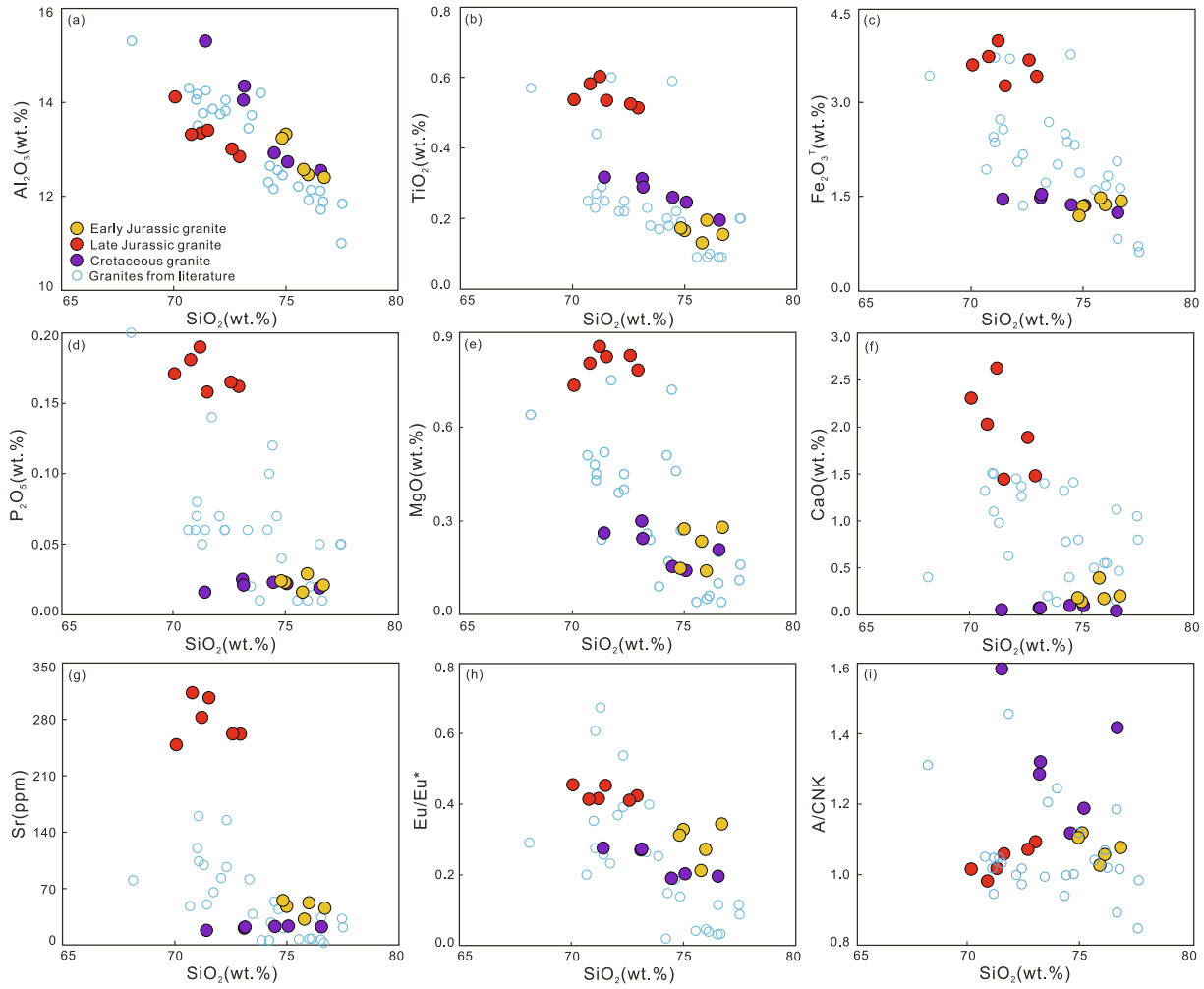

Fig. 8. Harker diagrams for the Mesozoic granites in the Bachi area. The data sources are same as the Fig. 7.

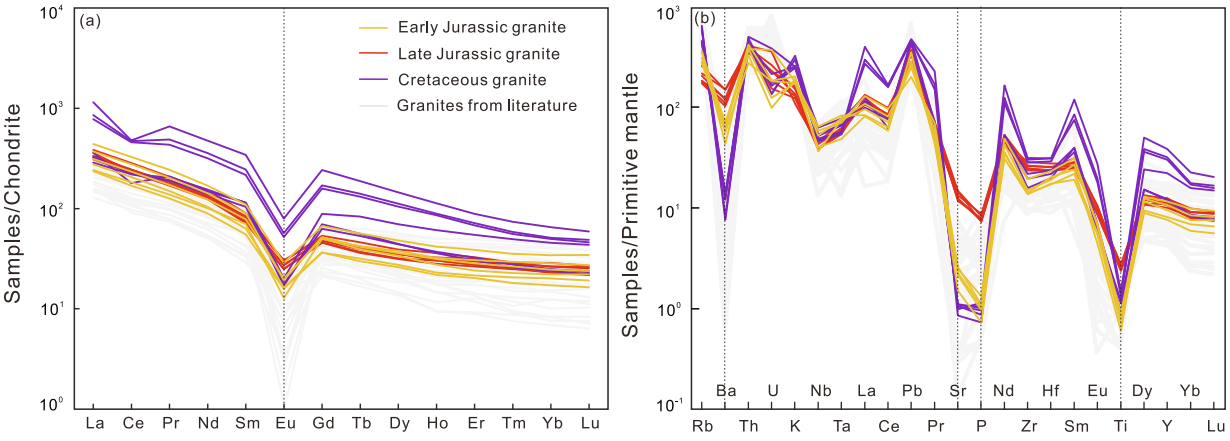

Fig. 9. Normalized (a) REE patterns and (b) trace element diagrams for the Mesozoic granites in the Bachi area. Normalized values of primitive mantle and chondrite are from Sun and McDonough (1989). The data sources are same as the Fig. 7.

the Late Jurassic granite show variable $^{176}Hf/^{177}Hf$ ratios (0.281709–0.282565), $\varepsilon_{Hf}(t)$ (−14.2 to −3.3) and Hf-T_{DM2} values (1278–2615 Ma), while the rims show relatively consistent $^{176}Hf/^{177}Hf$ ratios (0.282365–0.282506), $\varepsilon_{Hf}(t)$ (−11.1 to −6.1), and Hf-T_{DM2} values (1410–1687 Ma). The zircons form the Cretaceous granite show $^{176}Hf/^{177}Hf$ ratios of 0.282586–0.282633, $\varepsilon_{Hf}(t)$ values ranging between −4.9 and −2.9, and Hf-T_{DM2} values between 1186 and 1278 Ma.

5. Discussion

5.1. Genetic type

These Mesozoic granites in the Bachi area can be classified as A-type granites because (1) they show relatively high contents of high field strength elements (HFSE), high Zr + Nb + Ce + Y values, and high Ga/Al

Table 3
Whole rocks Sr-Nd isotopic data for the granitic rocks in the Bachi area.

Samples	Age (Ma)	$^{87}Rb/^{86}Sr$	$^{87}Sr/^{86}Sr$	±2σ	$(^{87}Sr/^{86}Sr)_i$	$^{147}Sm/^{144}Nd$	$^{143}Nd/^{144}Nd$	±2σ	$(^{143}Nd/^{144}Nd)_i$	εNd(i)	T_{DM}	T_{2DM}
SK-5	189	9.97	0.733605	0.000007	0.706813	0.125873	0.512398	0.000005	0.512242	−3.0	1307	1212
SK-9	189	10.28	0.733925	0.000008	0.706307	0.125320	0.512397	0.000009	0.512242	−3.0	1300	1213
SK-12	189	11.18	0.735917	0.000007	0.705861	0.122733	0.512407	0.000005	0.512255	−2.7	1247	1192
BC-11	153	1.44	0.716271	0.000006	0.713149	0.114671	0.512097	0.000005	0.511982	−9.0	1621	1668
BC-13	153	1.30	0.716061	0.000006	0.713244	0.116178	0.512103	0.000005	0.511987	−8.9	1636	1661
BC-15	153	1.91	0.716931	0.000005	0.712784	0.121582	0.512100	0.000004	0.511979	−9.0	1737	1674
RJ-11	94					0.143254	0.512326	0.000004	0.512238	−5.4	1783	1335
RJ-13	94					0.135255	0.512330	0.000004	0.512247	−5.3	1594	1321
RJ-24	94					0.146433	0.512340	0.000006	0.512250	−5.2	1836	1316

$(^{87}Sr/^{86}Sr)_i$ and $\varepsilon_{Nd}(t)$ values are calculated at t = 266 Ma based on present-day $(^{147}Sm/^{144}Nd)_{CHUR} = 0.1967$ and $(^{143}Nd/^{144}Nd)_{CHUR} = 0.512638$. T_{2DM} values are calculated based on present-day $(^{147}Sm/^{144}Nd)_{DM} = 0.2137$ and $(^{143}Nd/^{144}Nd)_{DM} = 0.51315$. $\lambda_{Rb} = 1.42 \times 10^{-11}$ year^{-1} (Steiger and Jäger, 1977), $\lambda_{Sm} = 6.54 \times 10^{-12}$ year^{-1} (Lugmair and Marti, 1978).

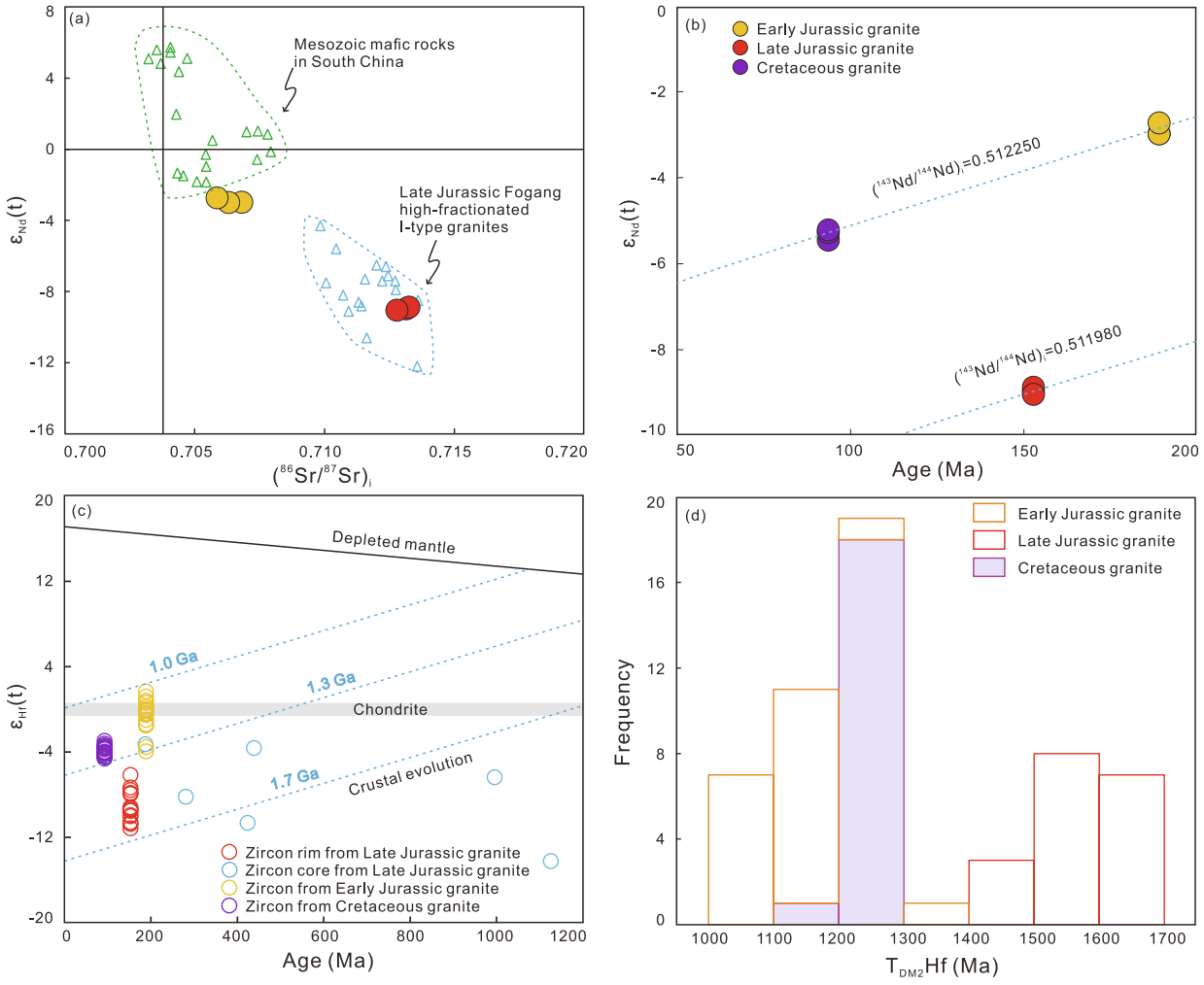

Fig. 10. Diagrams of (a) $\varepsilon_{Nd}(t)$ vs. I_{sr}, (b) $\varepsilon_{Nd}(t)$ vs. intrusive age for the samples and (c) $\varepsilon_{Hf}(t)$ vs. intrusive age, and (d) histogram Hf-T_{DM2} for the zircons from the Mesozoic granites in the Bachi area. The field for Mesozoic mafic rocks in South China is from Huang et al. (2013) and references therein. The samples for Late Jurassic Fogang high-fractionated I-type granites are from Li et al. (2007).

ratios (Fig. 11a-b), and (2) they are characterized by a strong depletion of Ba, Sr, P, Ti, and Eu (Fig. 9) possibly due to residual plagioclase in the magma source (Wu et al., 2002; Bonin, 2007; Zhang et al., 2012). Further, these Mesozoic granites have high SiO_2 and K_2O contents, which is also indicative for A-type granites (e.g. Wu et al., 2017).

The minimum T_{Zr} value for the Early Jurassic and Cretaceous granites that lack inherited zircon cores is 820 °C (Fig. 11c), suggesting high-temperature conditions for the initial magma for the Early Jurassic and Cretaceous granites. The T_{Zr} value for the Late Jurassic granite, which comprises abundant inherited/captured zircon cores is ~900 °C, and represents the initial magma temperature (Miller et al., 2003) (Fig. 11c). This temperature is similar to the high-temperature conditions for A-type granites. The survival of abundant inherited zircons in the Late Jurassic granite at high temperature can be explained by a fast crustal magma generation process (Bea et al., 2007). The correlation between $Al_2O_3 + MgO + TiO_2 + Fe_2O_3^T$ and $Al_2O_3/(MgO + TiO_2 + Fe_2O_3^T)$ indicates that all of the three Mesozoic granites was generated under a low-pressure condition (Fig. 11d). The high-temperature, low-pressure

Table 4
Zircon Hf isotopic data for the granitic rocks in the Bachi area.

Sample No	$^{176}Hf/^{177}Hf$	1σ	$^{176}Lu/^{177}Hf$	1σ	$^{176}Yb/^{177}Hf$	1σ	$\varepsilon_{Hf}(0)$	1σ	$\varepsilon_{Hf}(t)$	1σ	T_{DM1}	T_{DM2}	$f_{Lu/Hf}$
Early Jurassic biotite granite													
SK-1	0.282659	0.000020	0.001826	0.000050	0.064895	0.001610	−4.0	0.9	−0.1	0.9	858	1102	−0.95
SK-2	0.282631	0.000014	0.001097	0.000011	0.038812	0.000309	−5.0	0.7	−1.0	0.7	882	1153	−0.97
SK-3	0.282617	0.000009	0.001373	0.000025	0.050127	0.001123	−5.5	0.6	−1.5	0.6	908	1182	−0.96
SK-4	0.282665	0.000015	0.000660	0.000002	0.023586	0.000161	−3.8	0.7	0.3	0.7	824	1083	−0.98
SK-5	0.282557	0.000011	0.000464	0.000006	0.015897	0.000298	−7.6	0.6	−3.5	0.7	970	1294	−0.99
SK-6	0.282693	0.000013	0.001081	0.000007	0.038376	0.000359	−2.8	0.7	1.2	0.7	794	1031	−0.97
SK-8	0.282659	0.000013	0.001535	0.000018	0.054640	0.000407	−4.0	0.7	−0.1	0.7	853	1101	−0.95
SK-9	0.282621	0.000018	0.001775	0.000016	0.063108	0.000472	−5.3	0.8	−1.4	0.8	912	1177	−0.95
SK-10	0.282649	0.000009	0.001073	0.000015	0.039622	0.000525	−4.4	0.6	−0.3	0.6	856	1117	−0.97
SK-11	0.282654	0.000014	0.000971	0.000013	0.035050	0.000412	−4.2	0.7	−0.1	0.7	846	1106	−0.97
SK-12	0.282685	0.000021	0.002284	0.000212	0.093740	0.009636	−3.1	0.9	0.8	0.9	831	1054	−0.93
SK-13	0.282619	0.000015	0.001103	0.000007	0.040151	0.000417	−5.4	0.7	−1.4	0.7	899	1176	−0.97
SK-14	0.282644	0.000017	0.001015	0.000014	0.035583	0.000449	−4.5	0.8	−0.5	0.8	862	1127	−0.97
SK-16	0.282662	0.000016	0.001441	0.000017	0.053850	0.000682	−3.9	0.8	0.1	0.8	846	1095	−0.96
SK-17	0.282646	0.000013	0.000828	0.000009	0.028791	0.000450	−4.5	0.7	−0.4	0.7	854	1121	−0.98
SK-18	0.282679	0.000014	0.001888	0.000008	0.064583	0.000331	−3.3	0.7	0.6	0.7	830	1063	−0.94
SK-19	0.282666	0.000012	0.000975	0.000016	0.035062	0.000621	−3.8	0.7	0.3	0.7	830	1083	−0.97
SK-20	0.282709	0.000015	0.054721	0.000084	0.002813	0.002813	−2.2	0.7	1.7	0.7	783	1004	−0.95
SK-21	0.282546	0.000015	0.000753	0.000004	0.025943	0.000106	−8.0	0.7	−3.9	0.7	992	1316	−0.98
Late Jurassic biotite granite (zircon core)													
BC-3	0.281709	0.000011	0.002066	0.000036	0.069446	0.001522	−37.6	0.6	−14.2	0.7	2224	2615	−0.94
BC-9	0.281992	0.000015	0.001217	0.000009	0.042231	0.000175	−27.6	0.7	−6.4	0.8	1782	2085	−0.96
BC-11	0.282216	0.000010	0.001057	0.000006	0.037878	0.000058	−19.7	0.6	−10.6	0.7	1463	1871	−0.97
BC-19	0.282414	0.000013	0.002126	0.000015	0.071685	0.000766	−12.6	0.7	−3.6	0.7	1220	1496	−0.94
BC-22	0.282565	0.000012	0.000563	0.000002	0.019499	0.000149	−7.3	0.7	−3.3	0.7	961	1278	−0.98
BC-7	0.282372	0.000010	0.001055	0.000013	0.035720	0.000564	−14.2	0.6	−8.2	0.6	1245	1624	−0.97
Late Jurassic biotite granite (zircon rim)													
BC-2	0.282459	0.000013	0.001022	0.000003	0.033280	0.000263	−11.1	0.7	−7.8	0.7	1122	1504	−0.97
BC-4	0.282456	0.000009	0.000846	0.000011	0.028727	0.000349	−11.2	0.6	−7.9	0.6	1121	1508	−0.97
BC-6	0.282466	0.000008	0.000700	0.000008	0.021492	0.000155	−10.8	0.6	−7.6	0.6	1103	1489	−0.98
BC-8	0.282420	0.000016	0.001909	0.000090	0.065371	0.002978	−12.4	0.8	−9.3	0.8	1205	1584	−0.94
BC-10	0.282379	0.000016	0.001773	0.000031	0.059656	0.000969	−13.9	0.8	−10.7	0.8	1259	1664	−0.95
BC-12	0.282397	0.000016	0.000868	0.000010	0.027235	0.000243	−13.3	0.8	−10.0	0.8	1204	1625	−0.97
BC-15	0.282381	0.000012	0.000934	0.000003	0.028298	0.000166	−13.8	0.7	−10.6	0.7	1228	1656	−0.97
BC-16	0.282474	0.000015	0.001228	0.000006	0.039177	0.000248	−10.5	0.7	−7.3	0.7	1107	1475	−0.96
BC-18	0.282506	0.000015	0.000994	0.000007	0.033754	0.000175	−9.4	0.7	−6.1	0.7	1054	1410	−0.97
BC-20	0.282378	0.000011	0.000953	0.000011	0.028001	0.000273	−13.9	0.6	−10.7	0.7	1233	1661	−0.97
BC-21	0.282413	0.000008	0.001060	0.000082	0.036578	0.003043	−12.7	0.6	−9.4	0.6	1187	1593	−0.97
BC-23	0.282414	0.000017	0.002075	0.000050	0.071529	0.001526	−12.7	0.8	−9.5	0.8	1219	1597	−0.94
BC-24	0.282365	0.000011	0.001011	0.000001	0.033404	0.000120	−14.4	0.6	−11.1	0.6	1253	1687	−0.97
BC-26	0.282414	0.000022	0.001507	0.000058	0.046697	0.001898	−12.7	0.9	−9.5	0.9	1201	1595	−0.95
BC-27	0.282400	0.000013	0.001100	0.000011	0.036731	0.000530	−13.1	0.7	−9.9	0.7	1207	1619	−0.97
BC-28	0.282425	0.000013	0.002610	0.000079	0.087124	0.002732	−12.3	0.7	−9.2	0.7	1220	1578	−0.92
BC-29	0.282457	0.000018	0.001375	0.000029	0.045118	0.000849	−11.1	0.8	−7.9	0.8	1135	1509	−0.96
Late Cretaceous granite porphyry													
RJ-1	0.282603	0.000015	0.001254	0.000002	0.044516	0.000279	−6.0	0.7	−4.0	0.7	924	1245	−0.96
RJ-3	0.282628	0.000014	0.002445	0.000029	0.089733	0.001082	−5.1	0.7	−3.2	0.7	919	1201	−0.93
RJ-4	0.282593	0.000011	0.001272	0.000035	0.049286	0.001500	−6.3	0.6	−4.4	0.7	939	1265	−0.96
RJ-5	0.282595	0.000011	0.001034	0.000005	0.037917	0.000115	−6.3	0.7	−4.3	0.7	931	1261	−0.97
RJ-6	0.282599	0.000012	0.000808	0.000021	0.029143	0.000945	−6.1	0.7	−4.1	0.7	920	1253	−0.98
RJ-7	0.282620	0.000012	0.000907	0.000002	0.033471	0.000192	−5.4	0.7	−3.4	0.7	892	1211	−0.97
RJ-8	0.282617	0.000015	0.001461	0.000006	0.050354	0.000442	−5.5	0.7	−3.5	0.7	910	1219	−0.96
RJ-9	0.282604	0.000010	0.000980	0.000006	0.034199	0.000058	−5.9	0.6	−3.9	0.6	916	1242	−0.97
RJ-10	0.282602	0.000013	0.001191	0.000011	0.040688	0.000270	−6.0	0.7	−4.0	0.7	925	1247	−0.96
RJ-11	0.282620	0.000017	0.001416	0.000011	0.050109	0.000501	−5.4	0.8	−3.4	0.8	905	1213	−0.96
RJ-12	0.282614	0.000015	0.001241	0.000003	0.041707	0.000233	−5.6	0.7	−3.6	0.7	909	1224	−0.96
RJ-13	0.282590	0.000016	0.000844	0.000004	0.029986	0.000166	−6.4	0.8	−4.5	0.8	933	1270	−0.97
RJ-14	0.282611	0.000013	0.001304	0.000009	0.044993	0.000237	−5.7	0.7	−3.7	0.7	915	1230	−0.96
RJ-15	0.282586	0.000013	0.000951	0.000001	0.035231	0.000225	−6.6	0.7	−4.6	0.7	942	1278	−0.97
RJ-16	0.282601	0.000016	0.001666	0.000030	0.060613	0.001176	−6.0	0.8	−4.1	0.8	938	1250	−0.95
RJ-17	0.282594	0.000019	0.001710	0.000013	0.061981	0.000380	−6.3	0.8	−4.4	0.8	950	1265	−0.95
RJ-18	0.282633	0.000015	0.000866	0.000005	0.030527	0.000266	−4.9	0.7	−2.9	0.7	874	1186	−0.97
RJ-19	0.282613	0.000016	0.001273	0.000005	0.041772	0.000110	−5.6	0.8	−3.6	0.8	911	1225	−0.96
RJ-20	0.282590	0.000017	0.001021	0.000002	0.038729	0.000122	−6.4	0.8	−4.5	0.8	938	1271	−0.97

The parameter used in our calculations: $(^{176}Lu/^{177}Hf)_{CHUR} = 0.0332$, $(^{176}Hf/^{177}Hf)_{CHUR} = 0.282772$ (Blichert-Toft and Albarède, 1997); $(^{176}Lu/^{177}Hf)_{DM} = 0.0384$, $(^{176}Hf/^{177}Hf)_{DM} = 0.28325$ (Griffin et al., 2000); $\lambda(^{176}Lu) = 1.867 \times 10^{-11}$ a^{-1} (Söderlund et al., 2004). The $^{176}Lu/^{177}Hf$ (C) = 0.015 (Griffin et al., 2000).

conditions support the A-type classification of these Mesozoic granites (e.g. Anderson and Bender, 1989; Patiño Douce, 1997; Breiter, 2012).

5.2. Petrogenesis

Although all of the three Mesozoic plutons in the Bachi area belong to A-type granites, the Late Jurassic granite, however, shows different

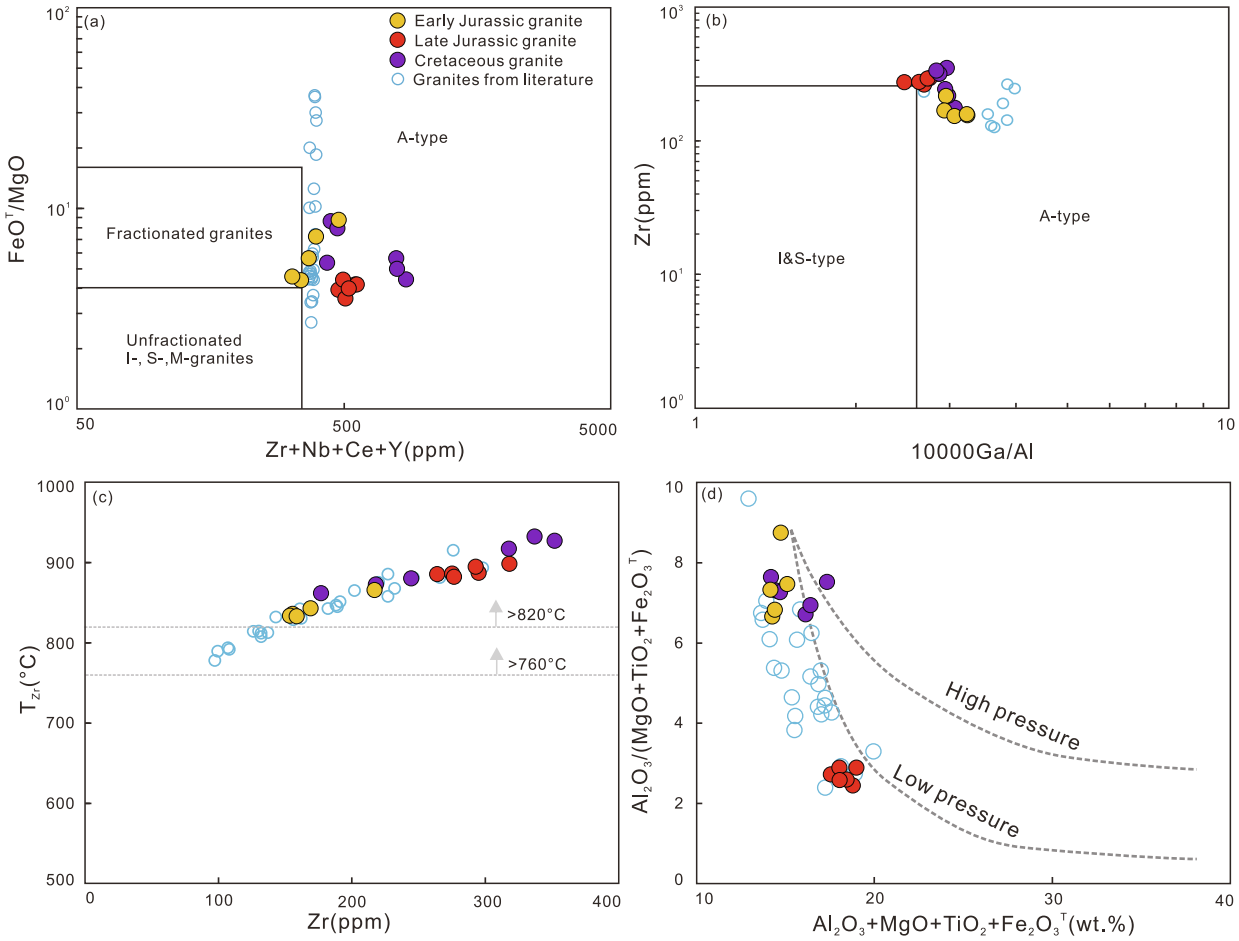

Fig. 11. (a) FeO^T/MgO vs. Zr + Nb + Ce + Y, (b) Zr vs. 10000 × Ga/Al diagrams (after Whalen et al., 1987), and (c) Zr saturation temperature (T_{Zr}) vs. Zr, and (d) $Al_2O_3/(MgO + TiO_2 + Fe_2O_3^T)$ vs. $Al_2O_3 + MgO + TiO_2 + Fe_2O_3^T$ (after Patiño Douce, 1999) for the Mesozoic granites in the Bachi area. T_{Zr} (°C) = 12900/(ln $D^{zircon/melt}$ + 0.85 M + 2.95) − 273.5, $D^{zircon/melt}$ = 496000/Zr contents in the melts (ppm), M = molar ratio of (Na + K + 2Ca)/(Al × Si) (Watson and Harrison, 1983). The data sources are same as the Fig. 7.

geochemical characteristics than the Early Jurassic and Cretaceous granites, i.e. the Late Jurassic granite shows lower K_2O, and higher CaO, Fe_2O_3, MgO contents, and more enriched isotopic compositions than the Early Jurassic and Cretaceous granites (Figs. 7–10). Further, the Late Jurassic granite comprises abundant inherited/captured zircon cores and REE-rich accessory minerals in contrast to the Early Jurassic and Cretaceous granites (Figs. 3 and 4). These differences indicate a different magma genesis for the Late Jurassic granite compared to the Early Jurassic and Cretaceous granites.

5.2.1. *Petrogenesis for the Early Jurassic and Cretaceous granites*

The Early Jurassic and Cretaceous granites show similar elemental and isotopic compositions (Figs. 7–10) indicating that they probably have the same magma source. Plausible models for generating A-type granites include: (1) evolution from a basaltic magma, including magmatic differentiation and magma mixing with a crust-derived magma (Turner et al., 1992; Frost et al., 1999). (2) Partial melting of felsic intrusions within the crust, including tonalite and granodiorite (Patiño Douce, 1997; Chen et al., 2020), or melting of granulite-facies metasedimentary rocks (Huang et al., 2011). (3) Partial melting of intermediate-mafic middle to lower crust that possibly underwent magmatic differentiation (Wu et al., 2002; Zhang et al., 2015a, 2015b). A granulite residue has also been suggested as a magma source for A-type granites (Collins et al., 1982; Clemens et al., 1986) but subsequent experimental data have shown that (1) it is difficult to develop granulite residues at high-temperature, low-pressure conditions (Bonin, 2007), and (2) dehydration melting of the shallow crust is unlikely to be the magma source as it is too refractory (Creaser et al., 1991; Patiño Douce, 1997). Experimental results also show that extensive fractional crystallization from mantle-derived mafic rocks is unlikely to be the source for A-type granites due to the high SiO_2 contents and high-temperature conditions for A-type granites (Clemens et al., 1986; King et al., 1997; King et al., 2001).

The Early Jurassic and Cretaceous granites have high SiO_2 (>71.0 wt %) and low MgO contents (<0.30 wt%), which excludes a mantle source. Generally, extensive mantle-derived mafic rocks would be expected if A-type granites were generated from an evolving basaltic magma (Sylvester, 1989; Sisson et al., 2005), but these are absent in the Bachi area. Contemporary asthenosphere-derived basaltic to andesitic rocks do occur in South China (Cen et al., 2016), but they show more depleted isotopic compositions than those of the A-type granites in this study (Fig. 10). Furthermore, the high Ce (>10 ppm) contents and the negative Eu anomaly (Fig. 4c) of the zircons also indicate that they derive from a crustal source rather than from mantle melting (e.g. Lei et al., 2013; Li et al., 2018). In addition, magma from melting of granulitic metasedimentary rocks usually displays high Al_2O_3 and low alkaline contents (Chappell and White, 1992; Deng et al., 2016), which is also inconsistent with those of the A-type granites in this study with high total alkaline values ($Na_2O + K_2O$ = 8.56–10.22 wt%). The Nd isotopic compositions (i.e. $\varepsilon_{Nd}(t)$ is −5.4 to −2.7) are also more depleted than those of regional meta-sedimentary rocks (i.e. $\varepsilon_{Nd}(t)$ = ~−12.0, Yuan et al., 1991; Jiang et al., 2009) and, therefore, exclude meta-sedimentary rocks as a magma

source.

Consequently, partial melting of igneous rocks including underplated mafic- intermediate rocks or felsic rocks could have been a possible magma source for the Early Jurassic and Cretaceous granites. A granitic magma derived from dehydration partial melting of mafic rocks should have similar major element compositions as calc-alkaline I-type granites, i.e. high Al_2O_3 and CaO contents, and a high Na_2O/K_2O ratio (Rapp and Watson, 1995). However, both the Early Jurassic and Cretaceous granites have low CaO contents (0.04–0.39 wt%), high K_2O contents (5.23–9.71 wt%), and low Na_2O/K_2O mass ratios (0.51–0.77), which are different from a magma derived from partial melting of mafic rocks (e.g. Wu et al., 2002; K_2O = 4 0.00–5.13 wt%; mass ratio Na_2O/K_2O = 0.85–1.20). Furthermore, coeval I-type granites, which were derived from the mafic rocks in continental crust, show more enriched Nd-Hf isotopic composition than those of the Early Jurassic and Cretaceous granites. This excludes mafic rock as a magma source for the Early Jurassic and Cretaceous A-type granites (Li et al., 2007, Fig. 10a).

The high K_2O contents, high K_2O/Na_2O ratios, and low CaO, P_2O_5, and MgO contents of peraluminous A-type granites are consistent with the experimental studies that A-type granites were derived from partial melting of felsic crustal igneous rocks at mid-crustal levels (Patiño Douce, 1997; Du et al., 2018). Further, experimental studies have also shown that partial melting of a felsic igneous rocks under high-temperature, low-pressure conditions could generate aluminous A-type granites (Creaser et al., 1991; Patiño Douce, 1997; Chen et al., 2020), supporting the formation of the aluminous Early Jurassic and Cretaceous granites under high-temperature, low-pressure conditions (Fig. 11c, d). Early Palaeozoic felsic rocks are common in South China and some of them show similar isotopic composition as the Early Jurassic and Cretaceous granites (e.g. Xia et al., 2014), indicating their potential as a magma source for the Early Jurassic and Cretaceous granites. Therefore, we conclude that the Early Jurassic and Cretaceous A-type granites were derived from partial melting of felsic igneous rocks, which was possibly followed by some differentiation, to form the more evolved varieties characterized by relatively flat REE patterns (Fig. 9a).

5.2.2. Petrogenesis for the Late Jurassic granite

The Late Jurassic granite comprises old inherited/captured zircon cores (Fig. 4b) and shows high zircon saturation temperatures of ~900 °C, (Fig. 11c). This suggests that the Late Jurassic granite was formed as a result of a fast magmatic process, involving melting of the lower continental crust due to the heat input from underplated mantle-derived mafic magmas associated with asthenosphere upwelling (Bea et al., 2007). Evidence for Late Jurassic asthenosphere upwelling has been proved by studies on coeval mafic rocks (2006;; Chen et al., 2016). In addition, compared to the Early Jurassic and Cretaceous granites, the Late Jurassic granite is characterized by higher Fe_2O_3 and MgO contents, a lower K_2O content, and a lower Na_2O/K_2O ratio, indicating a more mafic magmatic source for the Late Jurassic granite. This interpretation is supported by the following geochemical characteristics: (1) The Late Jurassic granite shows a similar major elemental and Sr-Nd isotopic composition as the Fogang I-type granite, which has been derived from mafic igneous rocks (Fig. 10a) (Li et al., 2007). This implies that the Late Jurassic granite in the Bachi area may also have originated from a mafic crustal source. (2) The zircon Hf isotopic compositions for the Late Jurassic granite (i.e. $\varepsilon_{Hf}(t) = -11.1$ to -6.1) are similar to those of the mafic crust-derived Gangwei and Lunshui calc-alkaline I-type granites (Huang et al., 2013). (3) The linear trends in the SiO_2 vs Al_2O_3, SiO_2 vs CaO, and A/CNK diagrams (Fig. 8) may result from fractional crystallization of plagioclase during the magmatic evolution, which would have caused the rise of SiO_2 and total alkaline contents in the melt. Thus, the initial magma may have been equivalent to a granodioritic magma as some of the samples plot near the granodiorite-granite boundary in the SiO_2 vs $Na_2O + K_2O$ diagram (Fig. 7a), which indicate a more mafic magma source for the Late Jurassic granite. (4) The low $(Na_2O + K_2O)/(MgO + FeO^T + CaO)$ mass ratios (1.2–1.7) and high $Al_2O_3 + MgO + FeO^T + CaO$ values (18.5–20.8 wt%) also suggest a more mafic magma source (Douce, 1999).

5.3. Implications for REE enrichment

All of the three Mesozoic granites in the Bachi area are characterized by high ΣREE contents (281–1212 ppm, in most cases >400 ppm). These values are higher than the average ΣREE contents of the upper continental crust (170 ppm, Rudnick and Gao, 2003) and the ΣREE contents of granites in the Nanling area in South China (229 ppm, Zhang et al., 2015a).

With regards to the Early Jurassic and Cretaceous A-type granites, the absence of REE-rich minerals indicates that the magmatic evolution may be not the main reason for REE enrichment (Wu et al., 1990). The Early Jurassic and Cretaceous granite show a strong Eu, Sr, and Ba depletion. Considering that they were derived from a relatively shallow crustal source, it is unlikely that the strong Eu, Sr, and Ba depletion is related to extensive magmatic fractionation (Wu et al., 2017). Experimental petrological studies have shown that low Al_2O_3, Sr, Eu, and Ba contents, and high Ga/Al ratios in A-type granites are most likely the result from residual feldspar in the source due to the low-pressure, anhydrous conditions (Patiño Douce, 1997; Litvinovsky et al., 2000; Zhang et al., 2012). The high HFSE contents including Zr, Nb, and REE are usually associated with the melting of accessory minerals in the source area (Jia et al., 2009; Zhang et al., 2012), as the high temperature promotes melting of these accessory minerals (Collins et al., 1982; Skjerlie and Johnston, 1992). Moreover, the shallow, felsic crustal source of the Early Jurassic and Cretaceous granites is characterized by higher REE contents than those of the mafic crust (Rudnick and Gao, 2003). It is suggested that the granites could have inherited the high REE contents from the source material by partial melting (Wu et al., 1990). Therefore, REE enrichment in the Early Jurassic and Cretaceous A type granites can be explained by the high-temperature, low-pressure, anhydrous conditions, and the geochemical composition of the felsic magmatic source.

With regards to the Late Jurassic granite, the magmatic source is more mafic than the felsic source for Early Jurassic and Cretaceous granites. It is, therefore, unlikely that the Late Jurassic granite will have similar high REE contents as the Early Jurassic and Cretaceous granites. It has been demonstrated that the REE enrichment or depletion in calc-alkaline granitic rocks during magmatic evolution are controlled by restite accessory phases present during crystal-melt separation. Generally, REE enrichment results from crystal-melt separation prior to the crystallization of accessory phases, while REE depletion associated with whole-rock fractionation occurs at a later stage after the accessory phases started to crystallize (Sawka et al., 1984). There are abundant REE-rich accessory minerals (allanite, titanite, apatite and fluorite) in the Late Jurassic granite, indicating that these accessory minerals were not separated from the melt during the magmatic evolution. Therefore, the occurrences of these accessory minerals, especially extensive allanite, which is the main REE-hosted magmatic mineral (Hermann, 2002; Vlach and Gualda, 2007), could be the main reason for the high REE contents in the Late Jurassic granite and indicate REE enrichment during the magmatic evolution. Also, the abundant inherited zircon cores and high temperature conditions suggest that melt production was followed by fast magma transfer to upper crustal levels (Bea et al., 2007). The fast magmatic process prevented the fractional crystallization of these REE-rich minerals from the melts before crystal-melt separation, which resulted in REE enrichment of the Late Jurassic granite. The REE-rich minerals were likely either to have been altered to form secondary hydrothermal REE-bearing minerals or were almost completely broken down during weathering processes, allowing the formation of the ion-adsorption REE deposits (Sanematsu and Watanabe, 2016).

The generation of A-type granites in the continental crust has been related to an extensional tectonic setting (Whalen et al., 1987; Wu et al., 2017). The heat input from the underplated asthenosphere-derived

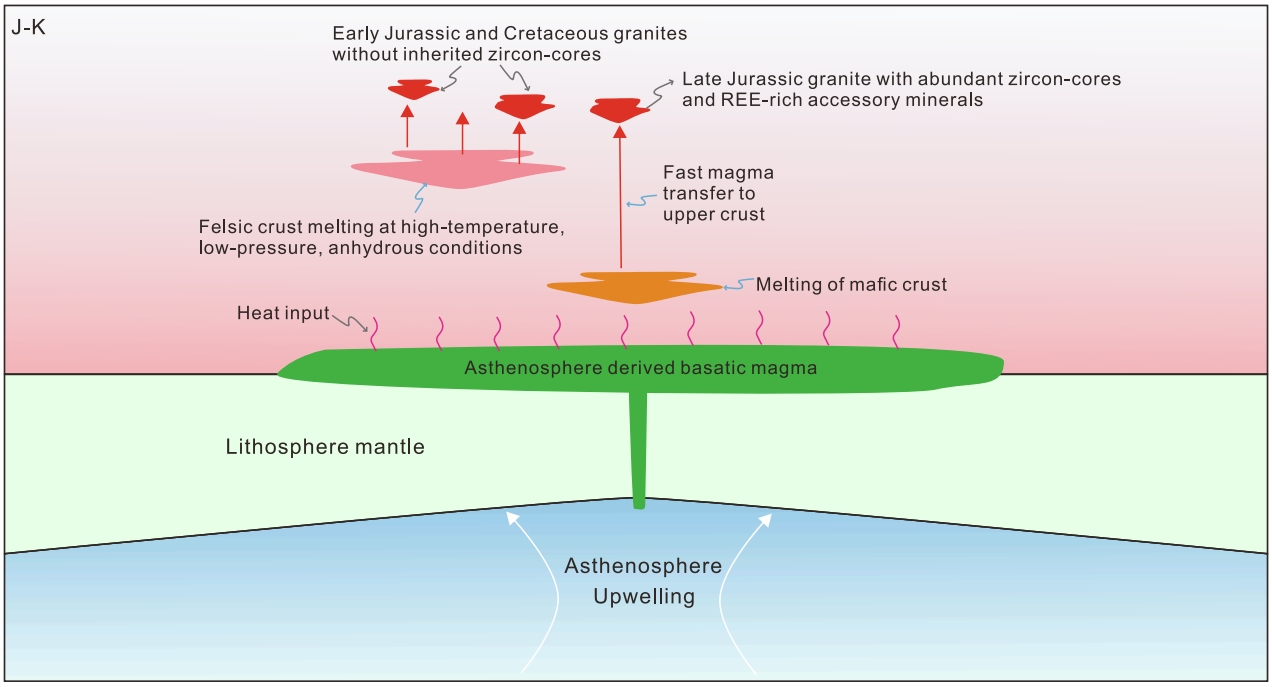

Fig. 12. Model for the generation of Mesozoic REE-rich A-type granites in South China.

basaltic magma in an extensional setting is crucial for crustal reworking (Bea, 2012; Yang et al., 2020). Furthermore, the high-temperature, low-pressure, anhydrous conditions are generally associated with an extensional tectonic setting, favouring the generation of the REE-rich granites. The fast crustal magma generation, which most likely caused the high REE contents in the Late Jurassic granite, occurred during extension where the heat was derived from underplated mantle-derived magma (Bea et al., 2007). Previous studies have demonstrated that South China was characterized by long-term asthenosphere upwelling and extension during the Mesozoic due to the slab foundering of the flat-subducted Paleo-Pacific plate beneath South China at 190–150 Ma (Li and Li, 2007; Li et al., 2007; Huang et al., 2013), and Late Jurassic to Cretaceous high-angle subduction induced by slab roll-back (Su et al., 2014; Deng et al., 2014; Chen et al., 2016). The Mesozoic extensional setting resulted in the generation of extensive A-type granitic rocks (Li and Li, 2007; Li et al., 2007; Wu et al., 2017). The high-temperature, low-pressure conditions, and the fast crustal magma generation in this extensional setting contributed to the REE enrichment in these A-type granites (Fig. 12).

6. Conclusions

The three Mesozoic A-type granites in the Bachi area yield zircon U-Pb ages of 189 Ma, 153 Ma and 94 Ma, respectively. They are characterized by high HFSE contents and the depletion of Eu, Sr, Ba, P, and Ti. The Early Jurassic and Cretaceous granites were derived from partial melting of felsic igneous rocks whereas the Late Jurassic granite was derived from partial melting of a more mafic source. These granites were generated under high-temperature, low-pressure, and anhydrous conditions related to Mesozoic extension in South China. These conditions were favourable for the generation of REE-rich granites. The felsic magma source resulted in high REE contents of the Early Jurassic and Cretaceous granites whereas fast magma generation processes caused REE enrichment in the Late Jurassic granite as there was not enough time for the separation of the REE-rich minerals from the melts before crystal-melt separation.

Declaration of Competing Interest

The authors declare that they have no known competing financial interests or personal relationships that could have appeared to influence the work reported in this paper.

Acknowledgments

We thank editor-in-chief Huayong Chen and associate editor Wei Terry Chen for handling our paper, and are grateful to two anonymous reviewers for their valuable comments that significantly improve our paper. This research was jointly supported by National Key R&D Program of China (No. 2017YFC0602301), Guangdong Major Project of Basic and Applied Basic Research, Grant No. 2019B030302013 and Technology Planning of Guangdong Province, China (NO. 2020B1212060055). We thank the valuable help from Jun Wang, Jingzhao Dou, and Yuzhou Feng during fieldwork. We also appreciate Dan Wu for her help with zircon U-Pb dating.

Appendix A. Supplementary data

Supplementary data to this article can be found online at https://doi.org/10.1016/j.oregeorev.2021.104317.

References

Anderson, J.L., Bender, E.E., 1989. Nature and origin of Proterozoic A-type granitic magmatism in the southwestern United States of America. Lithos 23, 19–52.
Bao, Z., Zhao, Z., 2008. Geochemistry of mineralization with exchangeable REY in the weathering crusts of granitic rocks in South China. Ore Geol. Rev. 33, 519–535.
Bao, Z.W., 1992. A geochemical study of the granitoid weathering crust in Southeast China. Geochimica 21, 166–174 (in Chinese with English abstract).
Bea, F., 2012. The sources of energy for crustal melting and the geochemistry of heat producing elements. Lithos 153, 278–291.
Bea, F., Montero, P., González-Lodeiro, F., Talavera, C., 2007. Zircon inheritance reveals exceptionally fast crustal magma generation processes in Central Iberia during the Cambro-Ordovician. J. Petrol. 48 (12), 2327–2339.
Blichert-Toft, J., Albarède, F., 1997. Separation of Hf and Lu for high-precision isotope analysis of rock samples by magnetic sector-multiple collector ICP-MS. Contrib. Mineral. Petrol. 127, 248–260.
Bonin, B., 2007. A-type granites and related rocks: Evolution of a concept, problems and prospects. Lithos 97, 1–29.

Breiter, K., 2012. Nearly contemporaneous evolution of the A-and S-type fractionated granites in the Krušné hory/Erzgebirge Mts., Central Europe. Lithos 151, 105–121.
Cen, T., Li, W.X., Wang, X.C., Pang, C.J., Li, Z.X., Xing, G.F., Zhao, X.L., Tao, J., 2016. Petrogenesis of early Jurassic basalts in southern Jiangxi Province, South China: implications for the thermal state of the Mesozoic mantle beneath South China. Lithos 256, 311–330.
Chappell, B.W., White, A.J.R., 1992. I- and S-type granites in the Lachlan Fold Belt. Earth Environ. Sci. Trans. R. Soc. Edinb. 83 (1–2), 1–26.
Chen, J.F., Jahn, B.M., 1998. Crustal evolution of Southeastern China: Nd and Sr isotopic evidence. Tectonophysics 284 (1–2), 101–133.
Chen, J.J., Fu, L.B., Wei, J.H., Selby, D., Zhang, D.H., Zhou, H.Z., Zhao, X.u., Liu, Y., 2020. Proto-Tethys magmatic evolution along northern Gondwana: insights from Late Silurian-Middle Devonian A-type magmatism, East Kunlun Orogen, Northern Tibetan Plateau, China. Lithos 356, 105304.
Chen, Y.X., Li, H., Sun, W.D., Ireland, T., Tian, X.F., Hu, Y.B., Yang, W.B., Chen, C., Xu, D. R., 2016. Generation of Late Mesozoic Qianlishan A2 -Type Granite in Nanling Range, South China: implications for Shizhuyuan W-Sn Mineralization and Tectonic Evolution. Lithos 266–267, 435–452.
Chi, R.A., Tian, J., Li, Z.J., Peng, C., Wu, Y.X., Li, S.R., Wang, C.W., Zhou, Z.R., 2005. Existing state and partitioning of rare earth on weathered ores. J. Rare Earths 23, 756.
Clemens, J.D., Holloway, J.R., White, A.J.R., 1986. Origin of an A-type granite: experimental constraints. Am. Mineral. 71, 317–324.
Collins, W.J., Beams, S.D., White, A.J.R., Chappell, B.W., 1982. Nature and origin -type granites with particular reference to Southeastern Australia. Contrib. Miner. Petrol. 80, 189–200.
Creaser, R.A., Price, R.C., Wormald, R.J., 1991. A-type granites revisited: assessment of a residual–source model. Geology 19, 163–166.
Deng, X.Q., Zhao, T.P., Peng, T.P., 2016. Age and geochemistry of the early Mesoproterozoic A–type granites in the southern margin of the North China Craton: constraints on their petrogenesis and tectonic implications. Precambr. Res. 283, 68–88.
Deng, Z.B., Liu, S.W., Zhang, L.F., Wang, Z.Q., Wang, W., Yang, P.T., Luo, P., Guo, B.R., 2014. Geochemistry, zircon U-Pb and Lu–Hf isotopes of an Early Cretaceous intrusive suite in northeastern Jiangxi Province, South China Block: implications for petrogenesis, crust/mantle interactions and geodynamic processes. Lithos 200, 334–354.
Douce, A.E.P., 1999. What do experiments tell us about the relative contributions of crust and mantle to the origins of granitic magmas? In: Castro, A., Fernandez, C., Vigneresse, J.L. (Eds.), Understanding Granites: Integrating New and Classical Techniques. Geological Society of London, Special Publications, pp. 55–75.
Du, L., Long, X.P., Yuan, C., Zhang, Y.Y., Huang, Z.Y., Sun, M., Xiao, W.J., 2018. Petrogenesis of Late Paleozoic diorites and A-type granites in the central Eastern Tianshan, NW China: Response to post–collisional extension triggered by slab breakoff. Lithos 318, 47–59.
Frost, B.R., Barnes, C.G., Collins, W.J., Arculus, R.J., Ellis, D.J., Frost, C.D., 2001. A geochemical classification for granitic rocks. J. Petrol. 42, 2033–2048.
Frost, C.D., Frost, B.R., Chamberlain, K.R., Edwards, B.R., 1999. Petrogenesis of the 1.43 Ga Sherman batholith, SE Wyoming, USA: a reduced, rapakivi–type anorogenic granite. J. Petrol. 40, 1771–1802.
Fu, W., Li, X.T., Feng, Y.Y., Feng, M., Peng, Z., Yu, H.X., Lin, H., 2019. Chemical weathering of s-type granite and formation of rare earth element (REE)-rich Regolith in South China: critical control of lithology. Chem. Geol. 520, 33–51.
Griffin, W.L., Pearson, N.J., Belousova, E., Jackson, S.E., van Achterbergh, E., O'Reilly, S. Y., Shee, S.R., 2000. The Hf isotope composition of cratonic mantle: LAM-MC-ICPMS analysis of zircon megacrysts in kimberlites. Geochim. Cosmochim. Acta 64, 133–147.
He, C., Xu, C., Zhao, Z., Kynicky, J., Song, W., Wang, L., 2017. Petrogenesis and mineralization of ree-rich granites in Qingxi and Guanxi, Nanling Region, South China. Ore Geol. Rev. 81, 309–325.
Hermann, J., 2002. Allanite: thorium and light rare earth element carrier in subducted crust. Chem. Geol. 192 (3–4), 289–306.
Hoskin, P.W.O., Schaltegger, U., 2003. The composition of zircon and igneous and metamorphic petrogenesis. In: Hanchar, J.M., Hoskin, P.W.O. (Eds.), Zircon: Reviews in Mineralogy and Geochemistry, pp. 27–62.
Hua, R.M., Zhang, W.L., Gu, S.Y., Chen, P.R., 2007. Comparison between REE granite and W-Sn granite in the Nanling region, South China, and their mineralization. Acta Petrol. Sinica 23 (10), 2321–2328 (in Chinese with English abstract).
Huang, H.Q., Li, X.H., Li, Z.X., Li, W.X., 2013. Intraplate crustal remelting as the genesis of Jurassic high-K granites in the coastal region of the Guangdong Province, SE China. J. Asian Earth Sci. 74, 280–302.
Huang, H.Q., Li, X.H., Li, W.X., Li, Z.X., 2011. Formation of high δ18O fayalite–bearing A–type granite by high–temperature melting of granulitic metasedimentary rocks, southern China. Geology 39 (10), 903–906.
Huo, M., 1992. Distribution characteristics of the weathering-crust-type rare-earth resources in Nanling, China. J. Nat. Resour. 7, 64–70 (in Chinese with English abstract).
Ishihara, S., Hua, R., Hoshino, M., Murakami, H., 2008. REE abundance and REE minerals in granitic rocks in the Nanling range, Jiangxi Province, southern China, and generation of the REE-rich weathered crust deposits. Resour. Geol. 58 (4), 355–372.
Janots, E., Bernier, F., Brunet, F., Muñoz, M., Trcera, N., Berger, A., Lanson, M., 2015. Ce (III) and Ce (IV)(re) distribution and fractionation in a laterite profile from Madagascar: insights from in situ XANES spectroscopy at the Ce LIII–edge. Geochim. Cosmochim. Acta 153, 134–148.
Jia, X.H., Wang, Q., Tang, G.J., 2009. A-type granites: research progress and implications. Geotectonica Metallogenia 33 (3), 465–480 (in Chinese with English abstract).
Jiang, X.Y., Li, X.H., Collins, W.J., Huang, H.Q., 2015. U-Pb age and Hf-O isotopes of detrital zircons from Hainan Island: Implications for Mesozoic subduction models. Lithos 239, 60–70.
Jiang, Y.H., Jiang, S.Y., Dai, B.Z., Liao, S.Y., Zhao, K.D., Ling, H.F., 2009. Middle to late Jurassic felsic and mafic magmatism in southern Hunan province, southeast China: implications for a continental arc to rifting. Lithos 107, 185–204.
King, P.L., White, A.J.R., Chappell, B.W., Allen, C.M., 1997. Characterization and origin of aluminous A–type granites from the Lachlan Fold Belt, Southeastern Australia. J. Petrol. 38 (3), 371–391.
King, P.L., Chappell, B.W., Allen, C.M., White, A.J.R., 2001. Are A-type granites the high–temperature felsic granites? Evidence from fractionated granites of the Wangrah Suite. Aust. J. Earth Sci. 48, 501–514.
Lei, W.Y., Shi, G.H., Liu, Y.X., 2013. Research progress on trace element characteristics of zircons of different origins. Earth Sci. Front. 20, 1–12.
Li, X.H., Chen, Z., Liu, D., Li, W.X., 2003. Jurassic gabbro-granite-syenite suites from Southern Jiangxi Province, SE China: age, origin, and tectonic significance. International Geology Review 45 (10), 898–921.
Li, C.Y., Zhang, H., Wang, F.Y., Liu, J.Q., Sun, Y.L., Hao, X.-L., Li, Y.L., Sun, W., 2012. The formation of the Dabaoshan porphyry molybdenum deposit induced by slab rollback. Lithos 150, 101–110.
Li, H., Myint, A.Z., Yonezu, K., Watanabe, K., Algeo, T.J., Wu, J.H., 2018. Geochemistry and U-Pb geochronology of the Wagone and Hermyingyi A-type granites, southern Myanmar: Implications for tectonic setting, magma evolution and Sn–W mineralization. Ore Geol. Rev. 95, 575–592.
Li, X.H., Li, W.X., Li, Z.X., Liu, Y., 2008. 850–790 Ma bimodal volcanic and intrusive rocks in northern Zhejiang, South China: a major episode of continental rift magmatism during the breakup of Rodinia. Lithos 102 (1–2), 341–357.
Li, X.H., Li, Z.X., Li, W.X., Liu, Y., Yuan, C., Wei, G.J., Qi, C.S., 2007. U-Pb zircon, geochemical and Sr–Nd–Hf isotopic constraints on age and origin of Jurassic I and A-type granites from central Guangdong, SE China: a major igneous event in response to foundering of a subducted flat-slab? Lithos 96, 186–204.
Li, Y.H.M., Zhao, W.W., Zhou, M., 2017. Nature of Parent Rocks, Mineralization Styles and Ore Genesis of Regolith-Hosted REE Deposits in South China: an Integrated Genetic Model. J. Asian Earth Sci. 148, 65–95.
Li, Z.X., Li, X.H., 2007. Formation of the 1300-km-wide intracontinental orogen and postorogenic magmatic province in Mesozoic South China: a flat–slab subduction model. Geology 35 (2), 179–182.
Litvinovsky, B.A., Steel, I.M., Wickham, S.M., 2000. Silicic magma formation in overthickened crust: melting of charnockite and leucogranite at 15, 20 and 25 kbar. J. Petrol. 41 (5), 717–737.
Ludwig, K.R., 2003. In: ISOPLOT 3.00: A Geochronological Toolkit for Microsoft Excel. Berkeley Geochronology Center, California, Berkeley, p. 39.
Lugmair, G.W., Marti, K., 1978. Lunar initial 143Nd/144Nd: differential evolution of the lunar crust and mantle. Earth Planet. Sci. Lett. 39 (3), 349–357.
Maniar, P.D., Piccoli, P.M., 1989. Tectonic discrimination of granitoids. Geol. Soc. Am. Bull. 101 (5), 635–643.
Mao, J., Cheng, Y., Chen, M., Franco, P., 2013. Major types and time-space distribution of Mesozoic ore deposits in South China and their geodynamic settings. Miner. Deposita 48, 267–294.
Middlemost, E.A.K., 1985. Magmas and Magmatic Rocks: An Introduction to Igneous Petrology. Longman, London, pp. 1–266.
Miller, C.F., McDowell, S.M., Mapes, R.W., 2003. Hot and cold granites? Implications of zircon saturation temperatures and preservation of inheritance. Geology 31, 529–532.
Patiño Douce, A.E., 1997. Generation of metaluminous A-type granites by low–pressure melting of calc–alkaline granitoids. Geology 25, 743–746.
Pei, Q., Liu, T., Yuan, H., Cao, H., Li, S., Hu, X., 2015. Geochemical characteristics of trace elements of ion adsorption type rare earth elements deposit in Guposhan region, Guangxi, China. J. Chengdu Univ. Technol. (Science & Technology Edition) 42, 451–462 (in Chinese with English abstract).
Polat, A., Hofmann, A.W., 2003. Alteration and geochemical patterns in the 3.7–3.8 Ga Isua greenstone belt, West Greenland. Precambr. Res. 126 (3), 197–218.
Rapp, R.P., Watson, E.B., 1995. Dehydration melting of metabasalt at 8–32 kbar: implications for continental growth and crust-mantle recycling. J. Petrol. 36 (4), 891–931.
Rocha, A., Schissel, D., Sprecher, A., de Tarso, P., Goode, J., 2013. Process development for the serra verde weathered crust elution-deposited rare earth deposit in Brazil. In: London, I., Goode, J., Moldoveanu, G., Rayat, M. (Eds.), Rare Earth Elements — Proceedings of the 52nd Conference of Metallurgists (COM 2013). Metallurgical Society of the Canadian Institute of Mining, Metallurgy and Petroleum (MetSoc-CIM), Montreal, Canada.
Rudnick, R.L., Gao, S., 2003. Composition of the continental crust. Treat. Geochem. 3, 1–64.
Sanematsu, K., Kon, Y., Imai, A., Watanabe, K., Watanabe, Y., 2013. Geochemical and mineralogical characteristics of ion–adsorption type REE mineralization in Phuket, Thailand. Miner. Deposita 48, 437–451.
Sanematsu, K., Watanabe, Y., 2016. Characteristics and genesis of ion adsorption-type rare earth element deposits. Rev. Econ. Geol 18, 55–79.
Sawka, W.N., Chappell, B.W., Norrish, K., 1984. Light-rare-earth-element zoning in sphene and allanite during granitoid fractionation. Geology 12 (3), 131–134.
Sawka, W.N., Chappell, B.W., 1988. Fractionation of uranium, thorium and rare earth elements in a vertically zoned granodiorite: implications for heat production

distributions in the sierra Nevada batholith, California, U.S.A. Geochim. Cosmochim. Acta 52 (5), 1131–1143.
Shu, L.S., 2006. Predevonian Tectonic Evolution of South China: from Cathaysian Block to Caledonian Period Folded Orogenic Belt. Geol. J. China Univ. 12, 418–431 (in Chinese with English abstract).
Sisson, T.W., Ratajesti, K., Hankins, W.B., Glazner, A.F., 2005. Voluminous granitic magmas from common basaltic sources. Contrib. Miner. Petrol. 148, 635–661.
Skjerlie, K.P., Johnston, A.D., 1992. Vapor-absent melting at 10 kbar of a biotite-and amphibole-bearing tonalitic gneiss: implications for the generation of A-type granites. Geology 20 (3), 263–266.
Söderlund, U., Patchett, P.J., Vervoort, J.D., Isachsen, C.E., 2004. The 176Lu decay constant determined by Lu–Hf and U-Pb isotope systematics of Precambrian mafic intrusions. Earth Planet. Sci. Lett. 219, 311–324.
Steiger, R.H., Jäger, E., 1977. Subcommission on geochronology: convention on the use of decay constants in geo- and cosmochronology. Earth Planet. Sci. Lett. 36 (3), 359–362.
Su, H.M., Mao, J.W., Santosh, M., Xie, G.Q., 2014. Petrogenesis and tectonic significance of Late Jurassic-Early Cretaceous volcanic-intrusive complex in the Tianhuashan basin, South China. Ore Geol. Rev. 56, 566–583.
Sun, S.S., McDonough, W.F., 1989. Chemical and isotopic systematics of oceanic basalts: implications for mantle composition and processes. Geol. Soc. Lond. Spec. Publ. 42 (1), 313–345.
Sylvester, P.J., 1989. Post–collisional alkaline granites. J. Geol. 97, 261–280.
Tanaka, T., Togashi, S., Kamioka, H., Amakawa, H., Kagami, H., Hamamoto, T., 2000. Jndi–1: a neodymium isotopic reference in consistency with lajolla neodymium. Chem. Geol. 168 (168), 279–281.
Tang, J., Johannesson, K.H., 2010. Rare earth elements adsorption onto Carrizo sand: influence of strong solution complexation. Chem. Geol. 279, 120–133.
Tao, J., Li, W., Wyman, D.A., Wang, A., Xu, Z., 2018. Petrogenesis of Triassic Granite from the Jintan Pluton in Central Jiangxi Province, South China: Implication for Uranium Enrichment. Lithos 320–321, 62–74.
Thirlwall, M.F., 1991. Long–term reproducibility of multicollector Sr and Nd isotope ratio analysis. Chem. Geol. 94 (2), 85–104.
Tian, J., Yin, J., Chi, R., Rao, G., Jiang, M., Ouyang, K., 2010. Kinetics on leaching rare earth from the weathered crust elution-deposited rare earth ores with ammonium sulfate solution. Hydrometallurgy 101, 166–170.
Turner, S.P., Foden, J.D., Morrison, R.S., 1992. Derivation of some A–type magmas by fractionation of basaltic magma: an example from the Padthaway Ridge, South Australia. Lithos 28 (2), 151–179.
Vlach, S.R., Gualda, G.A., 2007. Allanite and chevkinite in A-type granites and syenites of the Graciosa Province, southern Brazil. Lithos 97 (1–2), 98–121.
Wang, J., Ruan, D., 1989. Evolution and RE concentration of Heling-type RE acidic volcanic rock series. J. Chinese Rare Earth Soc. 7, 68–72 (in Chinese with English abstract).
Wang, L., Xu, C., Zhao, Z., Song, W., Kynicky, J., 2015. Petrological and geochemical characteristics of Zhaibei granites in Nanling region, Southeast China: implications for REE mineralization. Ore Geol. Rev. 64, 569–582.
Watson, E.B., Harrison, T.M., 1983. Zircon saturation revisited: temperature and composition effects in a variety of crustal magma types. Earth Planet. Sci. Lett. 64, 295–304.
Whalen, J.B., Currie, K.L., Chappell, B.W., 1987. A-type granites: geochemical characteristics, discrimination and petrogenesis. Contrib. Miner. Petrol. 95 (4), 407–419.
Wilson, M., 1989. In: Igneous Petrogenesis: A Global Tectonic Approach. Chapman & Hall, London, pp. 13–34.
Wu, C.Y., Huang, D.H., Guo, Z., 1990. REE geochemistry in the weathered crust of granites, Longnan area, Jiangxi Province. Acta Geol. Sin. (English Edition) 193–209.
Wu, F.Y., Liu, X.C., Ji, W.Q., Wang, J.M., Yang, L., 2017. Highly fractionated granites: Recognition and research. Sci. China Earth Sci. 60, 1201–1219.
Wu, F.Y., Sun, D.Y., Li, H.M., Jahn, B.M., Wilde, S., 2002. A-type granites in northeastern China: age and geochemical constraints on their petrogenesis. Chem. Geol. 287, 143–173.
Xia, Y., Xu, X., Zou, H., Liu, L., 2014. Early Paleozoic crust–mantle interaction and lithosphere delamination in South China Block: evidence from geochronology, geochemistry, and Sr–Nd–Hf isotopes of granites. Lithos 184, 416–435.
Xie, Y., Hou, Z., Goldfarb, R.J., Guo, X., Wang, L., 2016. Rare earth element deposits in China. Rev. Econ. Geol. 18, 115–136.
Xu, C., Kynický, J., Smith, M.P., Kopriva, A., Brtnický, M., Urubek, T., Yang, Y.H., Zhao, Z., He, C., Song, W.L., 2017. Origin of heavy rare earth mineralization in South China. Nat. Commun. 8 (1), 1–7.
Yang, J.H., Zhang, J.H., Chen, J.Y., Sun, J.F., 2020. Mesozoic continental crustal rejuvenation of South China: Insights from zircon HfO isotopes of early Jurassic gabbros, syenites and A-type granites. Lithos 105678.
Yang, W.B., Niu, H.C., Shan, Q., Sun, W.D., Zhang, H., Li, N.B., Jiang, Y.H., Yu, X.Y., 2014. Geochemistry of magmatic and hydrothermal zircon from the highly evolved Baerzhe alkaline granite: implications for Zr–REE–Nb mineralization. Miner. Deposita 49 (4), 451–470.
Yu, J., Zhang, C., O'Reilly, S.Y., Griffin, W.L., Ling, H., Sun, T., Zhou, X., 2018. Basement components of the Xiangshan-Yuhuashan area, South China: defining the boundary between the Yangtze and Cathaysia blocks. Precambr. Res. 309, 102–122.
Yuan, Z.X., Wu, L.S., Zhang, Z.Q., Ye, X.J., 1991. Study on Sm–Nd and Rb–Sr isotopic age of the Mayuan Group in Northern Fujian. Acta Petrol. Mineral. 10, 127–132 (in Chinese with English abstract).
Yusoff, Z.M., Ngwenya, B.T., Parsons, I., 2013. Mobility and fractionation of REEs during deep weathering of geochemically contrasting granites in a tropical setting, Malaysia. Chem. Geol. 349, 71–86.
Zhang, L., Wu, K.X., Chen, L.K., Zhu, P., Ouyang, H., 2015a. Metallogenic Features of Ion-adsorption Type REE Deposits in Southern Jiangxi Province. J. Chinese Soc. Rare Earths 33 (1), 10–17 (in Chinese with English abstract).
Zhang, Q., Ran, H., Li, C.D., 2012. A-type granite: what is the essence? Acta Petrol. Mineral. 31 (4), 621–626 (in Chinese with Englishe abstract).
Zhang, X.H., Yuan, L.L., Xue, F.H., Yan, X., Mao, Q., 2015b. Early Permian A-type granites from central Inner Mongolia, North China: magmatic tracer of post-collisional tectonics and oceanic crustal recycling. Gondwana Res. 28 (1), 311–327.
Zhang, Z., Zheng, G., Takahashi, Y., Wu, C., Zheng, C., Yao, J., Xiao, C., 2016. Extreme enrichment of rare earth elements in hard clay rocks and its potential as a resource. Ore Geol. Rev. 72, 191–212.
Zhao, X., Fu, L.B., Wei, J.H., Bagas, L., Santosh, M., Liu, Y., Zhang, D.H., Zhou, H.Z., 2019. Late Permian back-arc extension of the eastern Paleo-Tethys Ocean: evidence from the East Kunlun Orogen, northern Tibetan Plateau. Lithos 340–341, 34–48.
Zhao, Z., Wang, D.H., Chen, Z.Y., Guo, N.X., Liu, X.X., He, H.H., 2014. Metallogenic Specialization of Rare Earth Mineralized Igneous Rocks in the Eastern Nanling Region. Geotectonica Metall. 38 (2), 255–263 (in Chinese with English abstract).
Zhou, X.M., Sun, T., Shen, W.Z., Shu, L.S., Niu, Y.L., 2006. Petrogenesis of Mesozoic granitoids and volcanic rocks in South China: a response to tectonic evolution. Episodes 29, 26.